LBNL-41787

ERNEST ORLANDO LAWRENCE
BERKELEY NATIONAL LABORATORY

Small Scale Processes and Entrainment in a Stratocumulus Marine Boundary Layer

David E. Stevens, Ann S. Almgren, John B. Bell,
Vince E. Beckner, and Charles A. Rendleman

Computing Sciences Directorate

May 1998

REFERENCE COPY
Does Not
Circulate

Bldg. 50 Library - Ref.
Lawrence Berkeley National Laboratory

LBNL-41787
Copy 1

DISCLAIMER

This document was prepared as an account of work sponsored by the United States Government. While this document is believed to contain correct information, neither the United States Government nor any agency thereof, nor the Regents of the University of California, nor any of their employees, makes any warranty, express or implied, or assumes any legal responsibility for the accuracy, completeness, or usefulness of any information, apparatus, product, or process disclosed, or represents that its use would not infringe privately owned rights. Reference herein to any specific commercial product, process, or service by its trade name, trademark, manufacturer, or otherwise, does not necessarily constitute or imply its endorsement, recommendation, or favoring by the United States Government or any agency thereof, or the Regents of the University of California. The views and opinions of authors expressed herein do not necessarily state or reflect those of the United States Government or any agency thereof or the Regents of the University of California.

Small Scale Processes and Entrainment in a Stratocumulus Marine Boundary Layer. *

David E. Stevens, Ann S. Almgren, John B. Bell,
Vince E. Beckner, and Charles A. Rendleman

Lawrence Berkeley National Laboratory
University of California
Berkeley, CA 94720, USA

Abstract

Lack of resolution is a common problem hampering the use of large eddy simulation models for investigating boundary layer dynamics. Entrainment into the tops of marine stratus is characteristic of this problem. The use of parallel computing as a technique for resolving both boundary layer motions and the entrainment region enables the investigation of the interaction between the moist thermodynamics and turbulence in the entrainment region at very small length scales (dx = 8 m, dz = 4 m). This interaction results in heterogeneity at small scales which is important for correctly diagnosing the details of entrainment.

This study presents several numerical experiments at high resolution using a generalization of a 1995 GCSS (GEWEX Cloud System Studies) model intercomparison. Subtle details of the numerical algorithm are found to cause larger differences in entrainment than choice of subgrid model. A kinetic energy budget shows that even for very high resolution, numerical dissipation is usually larger than that produced by the subgrid model. However, the structure of eddies at the inversion is determined mainly by resolution with very little dependence on numerical representation. Inversion properties are converging as resolution approachs an undulation scale. Most of the mixing is confined within 100 meters of the inversion with entraining motions having an aspect ratio of 6 to 1.

1 Introduction

An important unresolved problem in many areas of boundary layer meteorology is the process of entrainment through a stratified inversion. Large eddy simulations are becoming increasingly popular and there is considerable debate about the ability of these models to resolve overturning at the inversion. This study uses very high resolution simulations to clarify the role of small scale structures in the entrainment process. In the process, the ability of large eddy simulation to resolve these structures has been studied.

These turbulence simulations have been consistently limited by the lack of sufficient computational resources and one of the largest sources of error in large eddy simulation (LES) is the lack of resolution. To avoid the computational requirements of 3D modeling, there have been many investigations of idealized entrainment, often in 2D (MacVean and Bretherton, 1998; Kuo and Schubert, 1988) and with idealized vortices (Siems et al. 1992). High performance computers have only recently been able to achieve adequate resolution. The lack of resolution compounds two fundamental problems with LES, numerical error on resolved scales and errors due to the lack of unrepresented scales. Attempts to mitigate these problems have resulted in improved numerics (Almgren et al., 1996; Stevens and Bretherton, 1997; Skamarock and Klemp, 1994)

*This work was supported by the Defense Special Weapons Agency IACRO98-3017, through the U. S. Department of Energy under Contract No. DE-AC03-76SF00098.

and sub-grid scale parameterizations (Mason and Brown, 1994; Mason and Brown, 1998; Deardorf, 1974). This study uses a novel combination of massively parallel computing and modern numerics to investigate stratocumulus entrainment.

Entrainment in model simulations can come from several sources: simulated overturning of material surfaces pulling air from the stratified free atmosphere into a well-mixed boundary layer, numerical diffusion inherent in the method of integration or explicitly added for monotonicity or stability, and parameterized sub-grid scale diffusion. Ideally entrainment in the model would be represented by inviscid motions that are overturning on resolved scales and which initiate a transfer of energy to a parameterized sub-grid scale inertial range. Often this is not the case and the resolution required for an inertial range is not present. This paper quantifies these effects on entrainment for a moist test case.

Often atmospheric flows contain intrinsic length scales which must be properly resolved for a simulation to be trusted. Such a length scale was introduced in Bretherton et al. (1998) and investigated in Stevens and Bretherton (1998) for a simplified smoke cloud. This length scale arises from typical accelerations caused by the density jump at the inversion and is often less than 5 m. This is much smaller than typical resolutions used in large eddy simulation. Stevens and Bretherton found that lack of resolution for the smoke cloud caused excessive numerical diffusion at cloud top and hence under-resolved simulations overentrained.

Determining the effects of numerical errors is a challenging task. Errors in entrainment due to numerical defects can be more subtle than excessive diffusion at the inversion. Often, techniques to limit undesirable numerical effects can limit the strength of eddies impinging on the inversion which could actually lower entrainment. This study uses kinetic energy dissipation to show that numerical dissipation can be much greater than that of the subgrid model. An investigation of the vertical velocity spectra is then used to evaluate differences in dissipation between different numerical approaches.

Parameterized diffusion at the fine scale end of a turbulent inertial range is usually described as the desired outcome of subgrid models. Often this is unfeasible, due to lack of resolution. Improving sub-grid models for underresolved 3D LES models is an important precursor to adequately modeling these clouds via 1D column parameterization in larger scale models. This study presents several very high-resolution simulations where inertial subrange scaling is present in the boundary layer and compares them to coarser simulations. Since a large fraction of entraining boundary layer eddies are unresolvable with typical resolutions, these high resolution simulations provide a new view of entraining eddies, whose diagnosed bulk properties can then be incorporated into such subgrid models. This is done through statistics derived from the thickness and variability of the inversion. This work supports much of the recent effort (Lock and MacVean, 1998; Lewellen and Lewellen, 1998; B. Stevens et al, 1998) to relate entrainment to boundary layer motions.

This paper is organized around analysis of small scale motions in marine stratocumulus. Its analysis is also applicable to other types of convective boundary layers. The research uses a generalization of the smoke cloud case (Bretherton et al, 1998) and extends results which came out of its intercomparison. In Section 2, we introduce a case study, typical measures of entrainment and the aspects of the large eddy simulation model which facilitate this investigation. The relationship of the entrainment to the boundary layer dynamics is investigated in section 3. In section 4, the structures determining the turbulence at the inversion are examined. Throughout this text, the importance of adequate resolution is demonstrated by the convergence of simulation properties as resolution is increased. In section 5, we present conclusions and future directions. Summaries of the model and its parallel implementation follow in the appendices.

2 Case Description

The simulations performed are generalizations of a 1995 GCSS (Bretherton et al. 1998) model intercomparison. The 1995 intercomparison was chosen to isolate the effect of longwave radiative cooling on entrainment, by removing condensation and virtual effects on buoyancy. This simplified model intercomparison and made possible comparisons with dry convective boundary layers whose turbulent properties are better understood and documented. The study presented here reintroduces these effects through an analogous moist case and compares this case to the earlier dry case.

The GCSS test case simulated a turbulent boundary layer underneath a strongly stratified inversion. Turbulence was driven solely from radiation, parameterized by a conserved radiatively active tracer that mimicked the effects of cloud radiative cooling. Effectively, the only difference between the compared models was their choice of numerical algorithm and subgrid model. It was found that even for a single class of three-dimensional LES models, entrainment rates and other statistics often differed by a factor of two. Further research indicated that entrainment in a smoke cloud behaved analogously to that of laboratory experiments. However, in simulations where the resolution was too coarse ($\Delta x = 50\text{m}, \Delta z = 25\text{m}$), entrainment was dominated by numerical diffusion. This diffusion was correlated to not resolving an undulation scale at the inversion.

The initial profiles and typical hourly averages for q_t and θ_l, the total water mixing ratio and liquid water virtual potential temperature respectively are shown in Figure 1. The jumps in q_t and θ_l are similar in magnitude to those observed in Nichols and Turton (1983), although the resultant cloud is deeper and thicker as seen by the profile of q_c in Figure 1, the mixing ratio of condensed water. The initial profiles were chosen to be smooth in both q_t and θ_l to insure that details of the initialization were resolved on the coarsest of the simulations. The radiative cooling S_{rad} which drives the simulations was parameterized as in the intercomparison and is described below. The winds were initially calm and no large scale forcings such as subsidence was applied. Motions were initiated via a perturbation in θ_l and turbulent kinetic energy e_{tke} consisting of a fixed sum of sine waves with random amplitudes and phases. The maximum amplitude of each wave was 0.1 K and $10^{-3} m^2/s^2$ respectively. The domain was 3.2 km wide in each horizontal dimension and 1.2 km high.

The relevance of the smoke cloud to a more realistic moist cloud is a useful extension of the GCSS intercomparison. For many stratus clouds, there is an additional source of turbulence from evaporative cooling. This cooling arises from evaporation caused by mixing of saturated boundary layer air at cloud top with unsaturated above inversion air. The mixtures are often less buoyant than their initial sources due to this evaporation. This study includes this effect by specifying inversion jumps in q_t and θ_l which for a given jump in θ_v, the virtual potential temperature, results in the greatest possible evaporative cooling without buoyancy reversal. This corresponds to a value of zero for the stability parameter D as defined by Siems et al. (1990) and 0.23 for the stability parameter K as defined by MacVean and Mason (1990). This jump in inversion values is on the border of the instability region specified by Randall (1973). The buoyancy of mixtures as a function of above inversion air fraction is shown in Figure 2. Although there is a 4 K jump in θ_v at the inversion, roughly 50% of the mixtures are neutrally buoyant with respect to the boundary layer. This is caused by evaporative cooling exactly cancelling the increase in potential temperature from mixing in above inversion air.

The model used in this study integrates a modified form of the the anelastic equations of Ogura and Phillips (1962). These equations are found by decomposing the Navier-Stokes equations into an isentropic base state ρ_0, the leftover mean environmental component in hydrostatic balance ρ_1, and a dynamic perturbation ρ_2.

$$\rho(x,y,z,t) = \rho_0(z) + \rho_1(z) + \rho_2(x,y,z,t) \tag{1}$$

This results in the system of equations:

$$\frac{\partial u_i}{\partial t} = -u_j \frac{\partial u_i}{\partial x_j} - \frac{\partial \Pi}{\partial x_i} + g\theta_v^{\#}\delta_{i3} + \frac{1}{\rho_0}\frac{\partial \tau_{ij}}{\partial x_j}, \tag{2}$$

$$\frac{\partial \theta_l^*}{\partial t} = -u_j \frac{\partial \theta_l^*}{\partial x_j} - \frac{1}{\rho_0}\frac{\partial}{\partial x_j}\rho_0 \overline{u_j' \theta_l^{*\prime}} - \frac{1}{\rho_0 C_{pd}\theta_0}\frac{\partial F_r}{\partial z} \tag{3}$$

$$\frac{\partial q_t}{\partial t} = -u_j \frac{\partial q_t}{\partial x_j} - \frac{1}{\rho_0}\frac{\partial}{\partial x_j}\rho_0 \overline{u_j' q_t'} \tag{4}$$

$$\frac{\partial}{\partial x_j}\rho_0 u_j = 0, \tag{5}$$

where Π is the perturbation pressure p_2/ρ_0, $\theta_l^* = (\theta_l - \theta_0)/\theta_0$ is a scaled liquid water potential temperature, and $\theta_v^{\#} = \theta_{v,2}/\theta_0$ is a scaled virtual potential temperature buoyancy term. Longwave radiation is

parameterized using a simple parameterization.

$$F_r(z) = F_r(H)\exp\left(-K_a\int_z^H \rho_0 q_c dz\right) \tag{6}$$

where H is the height of the domain. For these simulations, constant values of $F_r(H) = 100$ W/m^2 and $K_a = 10$ m^2/kg were used. This results in most of the radiative forcing being concentrated with 70 meters of the inversion as seen in Figure 1. Cloud water, q_c, is found by inverting Wexler's equations (Flatau et al, 1992) and precipitation is neglected. The subgrid stresses τ_{ij} and fluxes $(\overline{u_j'q_t'}, \overline{u_j'\theta_l^{*\prime}})$ are computed using a sub-grid model.

Theories describing turbulent motions require estimates of where the sources and sinks of turbulent energy originate and what determines their magnitude. Often the numerical dissipation in the resolved advection scheme is equivalent to that produced by the subgrid model. This raises the issue of to what degree is the mixing in a simulation determined by a physically meaningful energy cascade versus the extent to which it is fixed by the model's resolution and numerics. An attempt to resolve this issue requires analysis of the interaction between the model numerics and the subgrid-model. This case study uses two sub-grid models to isolate dependancies on the sub-grid model. The subgrid models used in this study are the turbulent kinetic energy (TKE) 1.5-order closure scheme (Mellor and Yamada 1974) and the Smagorinsky/Lilly 1.0-order scheme (Lilly, 1962; Smagorinsky, 1963).

The TKE scheme is derived from averaging the momentum equations about a length scale determined by the model resolution. It involves a prognostic equation for the sub-grid energy e_{tke} which includes terms for production by deformation and buoyancy and its dissipation.

$$\frac{\partial e_{tke}}{\partial t} + u_k\frac{\partial e_{tke}}{\partial x_k} = K_m\mathrm{Def}^2 + \frac{2}{\rho_0}\frac{\partial}{\partial x_k}\rho_0 K_m\frac{\partial e_{tke}}{\partial x_k} - K_h N^2 - c_\epsilon\frac{e_{tke}^{3/2}}{l} \tag{7}$$

Here, K_m is the eddy viscosity, $\mathrm{Def}^2 = \frac{\partial u_j}{\partial x_j}(\frac{\partial u_i}{\partial x_j} + \frac{\partial u_j}{\partial x_i})$ is the deformation, and N^2 is a local estimate of the Brunt-Vaisala frequency. The term $\frac{2}{\rho_0}\frac{\partial}{\partial x_k}\rho_0 K_m\frac{\partial e_{tke}}{\partial x_k}$ parameterizes triple moment terms. Eq. (7) contains the length scale assumptions:

$$K_h = c_h l e_{tke}^{\frac{1}{2}}, \tag{8}$$

$$K_m = c_m l e_{tke}^{\frac{1}{2}}, \tag{9}$$

$$l = (\Delta x\Delta y\Delta z)^{1/3}. \tag{10}$$

If one makes the additional assumption that e_{tke} is in local equilibrium,

$$0 = K_m\mathrm{Def}^2 - K_h N^2 - c_\epsilon\frac{e_{tke}^{3/2}}{l}, \tag{11}$$

this model reduces to the Smagorinsky sub-grid model

$$K_m = C_s^2 l^2\mathrm{Def}\sqrt{1 - Ri/Pr}, \quad C_s^4 = c_m^3/c_\epsilon. \tag{12}$$

An interesting property of the Smagorinsky sub-grid model is that for strong Richardson numbers, $Ri > Pr$, $e_{tke} = 0$, whereas for the TKE model, e_{tke} is often nonzero under identical conditions.

The numerical model used in this study were developed by Almgren et al. (1996) using an advection scheme and treatment of physical processes developed by Stevens and Bretherton (1997) and Smolarkiewicz and Margolin (1995). For a detailed description of the numerical model, see Stevens et al. (1998) which includes the treatment of adaptive mesh refinement. In this paper, we use a distributed memory single-level version of the adaptive algorithm. The parallel implementation strategy is discussed in Appendix A. It is a forward-in-time projection method using a 3rd order advection scheme for both velocity and scalar

advection. This advection scheme has better accuracy properties than many commonly used schemes in meteorological models. Common sources of error in many large eddy simulations are errors in the resolved advective fluxes which often produce unphysical extrema in the moisture fields such as q_t. This can be avoided in forward-in-time schemes via flux correction techniques. Most of these techniques are equivalent to slope-limiting, where the normal slope of the solution used in calculating an advective flux over a cell face is limited to eliminate pathological under/overshoots (Leveque 1992). Slope limiting is used for both q_t and θ_l for this reason; however, slope-limiting for the momentum is not required. Its use is similar to the spectral filtering and artificial viscosity techniques used to control noise at high wavenumbers, often at the expense of accuracy in lower wavenumbers. Several researchers (Mason and Brown, 1998; B. Stevens et al, 1998) have conjectured that by eliminating numerical noise with these filters, the sub-grid models often perform in a more meaningful manner. This investigation uses simulations with and without slope limiting to test this idea.

Kinetic energy, $e = u_i u_i/2$, is a useful quantity for analyzing whether mixing in the model arises from the numerics or the sub-grid model and for relating boundary layer motions to entrainment. This quantity satisfies the budget equation:

$$\frac{\partial e}{\partial t} = -u_j \frac{\partial e}{\partial x_j} - u_j \frac{\partial \Pi}{\partial x_j} + g w \theta_v^{\#} + \frac{u_i}{\rho_0} \frac{\partial \tau_{ij}}{\partial x_j}. \tag{13}$$

Due to the cell-centered forward-in-time implementation of the model, it is possible to construct discrete budgets of e as described in Appendix B. One can use this energy budget with zero residual to focus attention on the dissipation in the model's advection scheme. We define an energy residual with no resolved dissipation:

$$\left(\frac{\partial e}{\partial t} + \left(u_j \frac{\partial e}{\partial x_j} \right)_{conv} + u_j \frac{\partial \Pi}{\partial x_j} - g w \theta_v^{\#} - \frac{u_i}{\rho_0} \frac{\partial \tau_{ij}}{\partial x_j} \right) = S_{e,res} \tag{14}$$

where $\left(u_j \frac{\partial e}{\partial x_j} \right)_{conv}$ is evaluated in conservative form as the convergence of an energy flux. Since the budget is exact, this residual is equivalent to

$$\left(u_j \frac{\partial e}{\partial x_j} \right)_{model} - \left(u_j \frac{\partial e}{\partial x_j} \right)_{conv} = S_{e,res}. \tag{15}$$

One can think of this as the numerical energy dissipation in the model. An estimate of an eddy viscosity can be found from a first-order model:

$$S_{e,res} = -K_e(z) \mathrm{Def}^2 \tag{16}$$

This makes it possible to directly compare the numerical diffusion against that of the subgrid model, since the subgrid dissipation is modelled as $K_m \mathrm{Def}^2$. Although dissipation in a large eddy simulation is a complicated nonlinear process that often involves countergradient transport, this eddy viscosity was found to have similar magnitude and behavior to that determined by the sub-grid model. Hence it is a useful estimate of the numerical diffusion as a function of height. Understanding how changes in the representation of turbulence in the boundary layer affect boundary layer properties helps clarify the role of resolution.

Predicting entrainment or the rate at which a boundary layer deepens with time is fundamental to parameterizing them in climate studies. Entrainment in this study, denoted w_e, is defined as the rate at which the average height of the inversion layer rises. Our definition of the inversion layer is the region for which q_t takes on values ($7.5 \leq q_t \leq 8.5$ (g/kg)). The mean horizontal average of the thickness of this layer, denoted δz_{inv}, is used as a measure of inversion thickness which measures the region where the strongest mixing of inversion and boundary layer air occurs. The standard deviation of δz_{inv} is an indication of the degree to which entraining tongues of air thicken the mixing region. This is different than the estimate used in the GCSS intercomparison of determining the boundary layer height as the topmost layer of an intermediate value of the tracer. The standard deviation of that boundary layer height indicates the average undulation of the inversion and isn't necessarily correlated with entrainment events. Other statistics involving δz_{inv} are useful tools for examining the role of resolution in properly capturing the entrainment dynamics. By

computing statistics on clusters of neighboring gridpoints where δz_{inv} is much thicker than its horizontal average one can estimate the average area and number of entraining eddies. This provides useful information on the structure of these eddies.

A relationship between the magnitude of boundary layer motions and entrainment is a fundamental part of parameterizing the entrainment. This requires relating the kinetic energy budget to entrainment. The "efficiency" of the entrainment, as described by the parameterization

$$w_e/w^* = A/Ri \tag{17}$$

$$w^* = 2.5\int_0^{z_{inv}} g\overline{w'\theta_v^{\#}}\,dz \tag{18}$$

$$Ri = \frac{g z_{inv}\Delta\theta_v}{\theta_0 w^{*2}}, \tag{19}$$

is an appealing concept from the dry convective boundary layer that appears to often hold for the dry smoke cloud. The A parameter is controversial as an estimate of the efficiency as it has dependencies which arise from the distribution of radiative cooling and choice of numerics, resolution, and sub-grid model. However, it is useful for framing a discussion about the ability of a boundary layer to perform work as it relates the buoyancy flux at cloud top $(-w_e\Delta\theta_v)$ to a fraction A of the buoyancy production in the boundary layer.

Much effort has gone into developing and validating parameterizations such as Equation (17). Often LES studies have been used as the chief means for validating them in the absence of the wide range of observations needed. One of the issues that has arisen from these LES studies is whether an adequate resolution of the localized entraining eddies is more or less important than capturing other boundary layer effects correctly. A study by Lewellen (1998) suggests that properly resolving the ability of turbulence in the boundary layer to perform work is the key to accurately simulating the evolution of these clouds. Since this only requires resolving eddies which scale with the boundary layer height, much less resolution is required as compared to resolving fine scale entraining eddies. Another viewpoint arises from the idea that entrainment is mainly a function of the net source of kinetic energy (Lock and MacVean, 1998). This would indicate that it is sufficient to resolve the sources of kinetic energy to get meaningful entrainment. In this case study, the sources are limited to radiation with the bulk of it contained within 100 m of the inversion. This is still much larger than the entraining eddy length scale. A final viewpoint is that resolving entraining eddies is fundamental to an accurate simulation. By providing simulations, where all of these length scales are resolved, this study is able to help clarify the role of physical processes in determining the validity of parameterizations such as Eq. (17).

3 Relationship of entrainment to boundary layer dynamics

Several experiments were conducted using the simulations summarized in Table 1. These experiments enable the simultaneous comparison of resolution, resolved numerics and the sub-grid model. These simulations are named according to their relative resolution L (low), M (medium), H (high), V (very high) and the value of l used in the subgrid model. For direct comparison to the smoke cloud, simulations were performed where the buoyancy was replaced by $\theta_v^{\#} = (\theta_l - \theta_0)/\theta_0$. This results in a 7 K inversion similar to that used in the GCSS intercomparison, but with cloud water and radiation profiles similar to the moist case described above. The simulation acronyms are composed of whether they involve a smoke cloud (first letter S) versus a moist one, their numerical resolution (L,M,H,V), the value of l, whether slope limiting occured (S_) and the order of the turbulence closure scheme used. In this comparison of simulations, several statistics were computed as hourly averages centered at 2.5 hours of simulated time, at which point, the simulated turbulence had settled into a steady state with respect to its forcings. This is shown by the behavior of w^* as shown below. These statistics are presented in Table 2.

Table 2 shows three different entrainment rates, the obvious two between the moist and dry case and whether slope-limiting was applied to the velocities. Although, there is no net production of turbulence in the moist case, the evaporative cooling of mixed parcels causes a rapid increase in entrainment that is

much greater than would be expected from differences in inversion strength. The difference in entrainment caused by slope-limiting is shown in the top plot of Figure 3, where there are two groupings of inversion heights. This indicates the tendency of slope-limiting to smooth fields can weaken entrainment significantly. This numerical dependence of the entrainment rate is stronger than the resolution dependence as seen by the top plot of Figure 4. Increased resolution for the moist case raises entrainment. This is in contrast to the smoke simulations (**SL40_15, SM20_15, and SH10_15**) which exhibit similar behavior to the simuluations used in the GCSS intercomparison where higher resolution was found to reduce numerical diffusion and hence spurious entrainment. It was also found in the GCSS study that slope-limiting had the largest effect on entrainment rate while resolution and type of sub-grid model were of smaller importance. Since slope-limiting and flux corrected transport are two commonly used techniques, understanding this numerical choice is very important.

All of the simulations in Table 2 whether moist or dry have the same integrated buoyancy production, w^* even though they have widely varying entrainment rates. This is a reflection of the fact that the same amount and distribution of radiative cooling was applied in each case. In the bottom plot of Figure 3, w^* is plotted as a function of time for all of the moist simulations. This plot indicates that the buoyancy production has equilibrated after roughly 4000 s. The A parameter is compared in Table 2 and the bottom plot of Figure 4. This parameter for the smoke cloud is behaving as in Stevens and Bretherton 1998 with higher resolution limiting numerical diffusion and lowering A. This parameter for the moist case is 60% higher or 100% higher depending on slope-limiting with higher resolution actually increasing A. This indicates the entrainment closure, Eq. (17), is not easily used for actual stratocumulus, since the evaporative cooling appears to weaken the inversion making an unaltered $\Delta\theta_v$ an unsuitable choice for the inversion strength.

The relationship of buoyancy production in the boundary layer is different between the dry and moist cases. The buoyancy flux profiles for **H10_15** and **SH10_15** are shown in Figure 5. The entrainment buoyancy flux for the smoke cloud is well described by the entrainment rate and jump in θ_l at the inversion (dotted line). For the moist case (solid line), there is a very small negative entrainment buoyancy flux that is not well represented using the jump in θ_v. The reason for this can be seen by comparing the actual moist buoyancy flux against what the buoyancy flux would look like for the same values of $\overline{w'\theta_l'}$ and $\overline{w'q_t'}$ if the layer were dry $\overline{w'\theta_v^{\#}}_{dry}$ or completely saturated $\overline{w'\theta_v^{\#}}_{moist}$.

$$\begin{aligned}
\overline{w'\theta_v^{\#}}_{dry} &= \frac{g}{\theta_0}\left(\overline{w'\theta_l'} + \theta_0 0.608\overline{w'q_t'}\right) \\
\overline{w'\theta_v^{\#}}_{moist} &= \frac{g}{\theta_0}\left(\beta\overline{w'\theta_l'} + \left(\frac{L\beta}{C_{pd}T} - 1.0\right)\overline{w'q_t'}\right) \\
\beta &= \frac{1 + \theta_0 1.608\frac{dqvs}{dT}}{1 + \frac{L}{C_{pd}}\frac{dqvs}{dT}}
\end{aligned} \tag{20}$$

These buoyancy fluxes are shown by dashed and dash-dot lines respectively. The actual buoyancy flux is close to the saturated buoyancy flux throughout the boundary layer, but is constrained to lie between the saturated and unsaturated fluxes. The unsaturated buoyancy flux is similar to the smoke buoyancy flux with a sharp minima which is well determined by the jump in inversion θ and the entrainment rate. Since the moist and actual buoyancy fluxes don't have this property, large changes in entrainment will not cause buoyancy to consume much kinetic energy. This reduces the effectiveness of quantities such as w^* for diagnosing entrainment. This case study provides multiple simulations with the same inversion with clearly different w_e, but very similar w^*.

The preceding results indicate that the boundary layer turbulence depends primarily on the numerical details. However the profile of $\left(\overline{q_t'^2}\right)^{1/2}$ as shown in Figure 6 depends strongly on resolution. The higher resolution simulations have stronger q_t perturbations which are concentrated at the inversion between 740 and 780 m for the moist case. Notice the diffused nature of the coarsest simulations. It appears that most of the heterogeneity is concentrated within 100 m of the inversion. This profile is converging as resolution is increased, independent of the details of the numerics. This behavior is also seen in other statistics. Figure 7

shows the average boundary layer deformation and enstrophy (half the square of the vorticity). Notice that the boundary layer deformation and enstrophy for both dry and moist cases have the same dependence on resolution. These quantities are clearly resolution sensitive. The resolution dependence of enstrophy has been noticed in simulations in other scientific fields as well (Bell and Marcus, 1992; Chorin, 1986). There is a seeming contradiction in that some statistics such as variance of q_t at the inversion appear to be much more sensitive to resolution than algorithmic details, whereas the entrainment rate is more impacted by numerics. Some feature of the numerics must control boundary layer entrainment.

An illustration of the role of numerics and resolution is seen in the vertical velocity power spectra of Figure 8 and 9. All of the $128x128x96$ simulations are plotted in Figure 8. Figure 9 shows the simulations for all of the resolutions with the TKE model and no slope-limiting. In both figures, amplitudes at the highest wavenumbers fall off faster than $k^{-5/3}$. This may not be an undesirable feature, since most of these wavenumbers have wavelengths that are underresolved by the model grid. Mason and Brown (1998) present simulations whose spectra fall off faster than $k^{-5/3}$ yet perform better in other statistics than simulations whose spectra better approximate $k^{-5/3}$. Both figures have interesting spectra for those wavenumbers which are resolved by the criteria that they have wavelengths smaller than 200 m and greater than $4\Delta x$. The reference lines in both figures for demonstrating a $k^{-5/3}$ dependence have wavenumber extents determined by this criteria. The line in Figure 8 is taken from **M20_15** and the line in Figure 9 is from **V06_15**. Note that for the simulation **L40_15**, there is only one valid wavenumber which fits in this range. **L40_15** uses the resolution of the GCSS intercomparison and illustrates the extent to which resolution in LES studies has been limited. The choice of 200 m as an upper bound is one-fourth of the boundary layer height and is a generous estimate of the start of the inertial range.

For a given resolution, the boundary layer spectra are all very similar with respect to numerics at low numbers as shown in Figure 8, while at high wavenumbers the simulations with slope-limiting have increased dissipation. For scales which satisfy the resolution criteria, their amplitudes approximate $k^{-5/3}$. The slope-limited cases are much less active at high wavenumbers than the non-slope limited ones. Both choices of sub-grid model have similar effects at both the inversion and the boundary layer. At the inversion the spectra of slope-limited cases have much less power for all wavenumbers. When resolution is allowed to increase for fixed numerics, the amplitudes at higher wavenumbers increase at the expense of lower wavenumbers. This indicates that low wavenumbers are being forced spuriously by lack of resolution. Hence many of the motions that are considered resolved in low resolution simulations may be numerical artifacts. A similar result was found by Brown and Minion (1995) where lack of resolved high wavenumbers led to spurious low wavenumber vortices. This might explain the differences between the low resolution and high resolution plots of inversion depth δz_{inv} in Figure 14 which are discussed in the next section.

The importance of quantifying the role of numerical dissipation has been shown above. This was done by comparing the numerical dissipation, $S_{e,res}$, to that of the subgrid model, $K_m \mathrm{Def}^2$. The fraction of the total dissipation which is numerically generated rather than produced by the subgrid model is shown in Figure 10. For simulations with a subgrid model, but no slope-limiting, numerical dissipation is roughly two-thirds of the total. The simulations **L40S_15**, **M20S_15**, and **H10S_15** show that when both the slope-limiter and sub-grid model are active, the increased dissipation from the slope-limiter is offset by decreased dissipation from the sub-grid model.

A similar ratio is observed when one compares the eddy viscosity required to relate the dissipation rate to the deformation rate, Def^2 (Figure 7). The deformation rate and total dissipation are roughly constant throughout most of the boundary layer for all cases. The Def^2 profile is seen to vary strongly with resolution with a peak at the boundary layer top (not shown). This peak has a depth of 50-60 m for most resolutions which resembles the behavior in $\left(\overline{q_t'^2}\right)^{1/2}$. This resolution dependence causes the numerical viscosity K_e to behave in a similar manner to the sub-grid model eddy viscosity. In Figure 11, a comparison of numerical versus sub-grid eddy viscosities is presented. In the case where no sub-grid model was applied K_m was computed as a diagnostic. We see that in the boundary layer this estimate is roughly equivalent to that of the sub-grid model. At the inversion this estimate is 5-6 times that of the sub-grid model. This indicates that lack of resolution at the inversion and its effects on the numerics are controlling mixing at the inversion. The

numerical eddy viscosity depends strongly on slope-limiting in the boundary layer and at the inversion. The numerical eddy viscosities without slope-limiting are 75-80% of the cases with slope-limiting, independent of resolution. This might account for the difference in entrainment caused by the slope-limiting.

4 Turbulent motions at the inversion

The preceding section shows the simulation of the inversion layer depends on both resolution and numerics. The role of resolution is seen in typical cross sections of q_t after 2 hours of simulation. Figure 12 displays cross sections for **L40_15, M20_15, H10_15** and **VO6_15**. The resolution is shown by plotting each cell as a rectangle whose size is determined by resolution and color by cell value. Only at the finer resolutions is overturning of mixed values observed. Although the inversion is remarkably flat, most of the tongues of entraining fluid extend to depths of 50-100 meters. As resolution increases these tongues thin roughly linearly and their number increases. In Figure 13, the layer defining δz_{inv} is plotted. This figure illustrates that most of the inversion is composed of a thin layer that is shrinking to a scale of less than 10 meters. Regions where entraining tongues occur thicken to a depth of roughly 50 meters. The difference in appearance between Figures 12 and 13 is due to the entraining tongues being mixed past the cutoff value of 8.5 (g/kg). This difference reflects the choice of an inversion depth where the greatest amount of mixing occurs.

Resolution apparently determines the average thickness of the inversion and the size and number of downwellings. Snapshots of the inversion reflect the increase in variability with resolution. In Figure 14, snapshots of δz_{inv} after 2 hours of simulation are presented for **L40_15, M20_15, H10_15** and **VO6_15**. Downwellings are very broad and the separating inversion spaces are relatively thick for **L40_15**. For **VO6_15**, a strong cellular structure with many more downwellings separated by a thinner inversion is observed. The entraining features are much broader in **L40_15** than the higher resolution simulations which is probably due to these scales being inaccurately forced by lack of resolution at the higher wavenumbers. By calculating statistics on these snapshots for each minute of the third hour of simulation, it is possible to generate qualitative information about these structures.

A goal of this study is to identify the importance of different scales of motion in determining entrainment. Horizontal averages of δz_{inv} indicate the importance of fine vertical resolution as seen in Figure 15. One scale identified by Bretherton and Stevens and Bretherton is the undulation length scale

$$\delta z_u = z_{inv}/Ri \tag{21}$$

This scale for the high resolution moist cases is around 7 meters versus 4 for the smoke case (these values are tabulated in Table 2), reflecting the weaker inversion of the moist case. The standard deviation of δz_{inv} also shown in Table 2 illustrates that the moist case is much more efficiently producing downwelling at the inversion. The importance of resolving the undulation scale for simulating mixing at the inversion is seen by the convergence of δz_{inv} as the numerical resolution approaches δz_u. For the moist and dry cases, the inversion layer was observed to converge at roughly first-order as a function of l, with the moist case converging as:

$$\delta z_{inv} = (5.4) + (0.22)(l)^{(1.07)} \tag{22}$$

It appears δz_{inv} has converged the most for simulations **H10_15** and **V06_15** which have vertical/horizontal resolutions of 6.25/12.5 and 4/8 meters respectively. Since 5.4 m is very close to the 6.8 m observed for simulation **V06_15**. It appears that this simulation is very close to the converged value. Note that for **L40_15**, δz_u and δz_{inv} are much less than the mesh spacings, while for **V06_15** both quantities are about twice the vertical mesh spacing.

The thickness of the inversion identifies δz_u as an important vertical length scale. It remains to be determined if this vertical scale is also an important horizontal scale. In Figure 16, hourly statistics are computed on clusters of neighboring columns where δz_{inv} is greater than 50 m. For simulations such as **L40_15**, this is equivalent to 2 vertical mesh spacings. These statistics provide supporting evidence for the role of resolution rather than numerics in determining the structure of eddies at the inversion. One finds from this figure that the total area spanned by these clusters, their average area and their number are

strongly determined by resolution. An interesting result is that the average depth of these clusters is roughly constant around 75 meters. This is roughly twice the distance between the inversion height and the peak of the radiative cooling. Hence the depth of these clusters appears to be primarily related to the distribution of the radiative cooling.

One consequence of the increased number of clusters with resolution assuming an even distribution of downwellings is that the average event composed of a downwelling and its thin surrounding inversion shrinks from a horizontal extent of 800 meters to 450 meters as resolution is increased from $l = 40$ m to 6m. This results in an aspect ratio changing from 20-1 in the coarsest simulations to 6 to 1 for the finest simulation. This is an aspect ratio similar to Rayleigh convection between two plates. Since these eddies have a depth roughly constant with resolution that scales with the source of kinetic energy, it suggests that this source has an important scale to resolve. Although this is much larger than the undulation scale, it is only spanned by more than 5 gridpoints in the finest simulations.

5 Conclusions

Inversion structure is clearly a function of resolution. Entrainment in underresolved simulations is caused by much larger diffused features. Most mixing is confined to within 100 m of the inversion with entraining eddies becoming more isotropic as the resolution increases. Typical entraining eddies have a horizontal scale of 450 meters amd a vertical scale of 75 m for an aspect of 6 to 1.

The entrainment rate depends more strongly on the presence of slope-limiting than sub-grid model, hence this numerical detail is a fundamental concern. If the entraining eddies are confined to within 100 meters of the inversion where the sub-grid models have weak eddy viscosities, extra diffusion in the numerics appears to be the only factor reducing the ability of the boundary layer simulation to entrain.

The optimal choice of numerics and sub-grid model is still ambiguous. However, since these models are attempting to approximate very high Reynold's number flows, elimination of numerical diffusion such as slope-limiting seems preferable. Especially when the majority of dissipation is numerically driven. One can make observations about the use of Smagorinsky versus the TKE model. Although both the Smagorinsky and TKE models are of comparable complexity to implement, and the TKE model eliminates the assumption that subgrid motions are locally in equilibrium, both sub-grid models produce roughly the same amount of dissipation as resolution was increased. Smagorinsky appears preferable, since it has the advantage of eliminating the necessity of advecting an additional scalar.

The large number of high resolution simulations presented in this study show the importance of doing a large number of interrelated simulations rather than one unsupported simulation. Our eventual goal is to perform simulations with length scales of less than 2 meters (1000^3 meshes) in less than a day of computer time. This will enable a thorough investigation of these turbulence problems on a research timescale that is not limited by access to sufficient resolution and computing time.

The same technique for implementing distributed parallel computing as described in Appendix A is easily extendable to adaptive mesh refinement. By refining in the vertical about the important 200 meters where entrainment is occurring, while providing 10 meter resolution in the boundary layer, we will increase our resolution by 50% without any increases in computational costs over the **V06_15** simulation.

Acknowledgments

This work was supported by the Defense Special Weapons Agency IACRO98-3017, through the U. S. Department of Energy under Contract No. DE-AC03-76SF00098.

Appendix A: Parallel Implementation

Modern parallel computers are potential solutions to the lack of resolution in many atmospheric simulations. These computers have the potential to resolve an order of magnitude smaller scales than a uniprocesser without sacrificing domain size, thus greatly reducing many sources of error. The use of parallel computing has been hampered by lack of an easily usable programming model. This paper presents a programming model in a large eddy simulation context that greatly reduces the effort needed for distributed parallel computing.

The programming model used in these simulations is based on an Object-oriented library called **BoxLib** which greatly reduced the implementation difficulties. It is a small, flexible set of tools for manipulating block decomposed data. Due to space limitations, only a summary is presented; a more in depth presentation is given in (Rendleman et. al. 1998). The block decomposition of the domain is described by a few basic abstractions

- An IntVect represents a point in index space.
- A Box represents the lower and upper bounds of a region as two points in index space. It is associated with operations such as intersection and other bounds manipulation tasks.
- A BoxArray is an array of boxes that represents a block decomposition. This is used for the calculus of manipulating data between regions.

An illustration of how the decomposed domain is represented using these classes is shown in Figure 17. Associated with these geometric quantities are the container classes:

- An FArrayBox is a container for data associated with a Box. It is associated with copying data, simple arithmetic operations and passing data to Fortran application routines.
- A MultiFab is a container for data associated with a BoxArray. It contains the FArrayBoxes associated with the Boxes in a BoxArray.

Using the geometric objects Box and BoxArray, it is a simple process to construct and process the buffers used in message passing, even for complex grid configurations. In most instances, this is easily accomplished in a manner which makes the parallelism transparent to the user. The resulting code is easily maintained and modified on serial processors as well, due to its Single Program Multiple Data (SPMD) programming model implemented using BSPLib or MPI for the parallel communication. By managing the complexities through well-thoughout container classes, one eliminates much of the difficulty of parallel computing. This formalism allows routines that were developed to run on uniprocessors to be ported with small modifications to distributed memory multiprocessors.

This structure extends naturally to an adaptive simulation. Once the domain has been decomposed into subgrids, messages between grids are required to solve the model equations. It is a natural extension of the **BoxLib** message passing model to allow communication between grids of different resolution. All that is required is software for accumulating residuals on coarse-fine interfaces and synchronization steps between coarse and fine data.

This approach generalizes naturally to load balancing where certain regions of the domain require more work due to details in the physics. One approach is to adaptively section the domain into grids with roughly equal amounts of work. For instance, it is possible to cluster processors around regions where radiation and microphysics calculations dominate the computational workload.

Appendix B: Model Description

The model integrates the equations Eq. 2-5 in their conservative form

$$\frac{\partial \vec{U}}{\partial t} = -\frac{\nabla \cdot (\rho_0 \vec{U}\vec{U})}{\rho_0} - \nabla \Pi + g\theta_v^{\#}\vec{k} + H_{\vec{U}}, \tag{23}$$

$$\frac{\partial \theta^*}{\partial t} = -\frac{\nabla \cdot (\rho_0 \vec{U} \theta^*)}{\rho_0} + H_{\theta^*}, \tag{24}$$

$$\frac{\partial q_t}{\partial t} = -\frac{\nabla \cdot (\rho_0 \vec{U} q_t)}{\rho_0} + H_{q_t}, \tag{25}$$

$$\nabla \cdot (\rho_0 \vec{U}) = 0, \tag{26}$$

Here vector notation is used to clarify the manner in which advection and mass continuity are implemented and all sources such as the sub-grid model and radiation are combined into forcing terms $(H_{\vec{U}}, H_{\theta^*}, H_{q_t})$. These equations are discretized using cell-centered velocities and scalars in a forward-in-time manner.

$$\frac{\vec{U}^{n+1} - \vec{U}^n}{\Delta t} = -D^m(\vec{M}^m \vec{U}^a)/\rho_0 - G\Pi^{n+\frac{1}{2}} + (g/2)((\theta_v^\#)^n + (\theta_v^\#)^*)\vec{k} + (H_{\vec{U}}^n + H_{\vec{U}}^*)/2 \tag{27}$$

$$\frac{(\theta^*)^{n+1} - (\theta^*)^n}{\Delta t} = -D^m(\vec{M}^m (\theta^*)^a)/\rho_0 + (H_{\theta^*}^n + H_{\theta^*}^*)/2 \tag{28}$$

$$\frac{q_t^{n+1} - q_t^n}{\Delta t} = -D^m(\vec{M}^m q_t^a)/\rho_0 + (H_{q_t}^n + H_{q_t}^*)/2 \tag{29}$$

This discretization is presented in more detail with comparisons to simpler analytical flows by Almgren et al. (1998). The continuity constraint requires solving elliptic equations when computing $(\vec{M}^m, \vec{U}^{n+1}, \Pi^{n+\frac{1}{2}})$. The fields $(\vec{U}^a, (\theta^*)^a, q_t^a)$ represent values traced from the cell centers to the midpoints of cell faces at $t^{n+\frac{1}{2}}$ using a forward-in-time advection method described below. The midpoint momenta $\vec{M}^m = \rho_0 \vec{U}^m$ are centered on cell faces at $t^{n+\frac{1}{2}}$ and satisfy a cell-centered divergence constraint

$$D^m(\vec{M}^m) = 0 \tag{30}$$

often referred to as the Arakawa C grid (Arakawa 1974) divergence constraint. The cell-centered velocities $(\vec{U}^n, \vec{U}^{n+1})$ approximate a nodal centered divergence constraint D.

$$D(\rho_0 \vec{U}^{n+1}) \approx 0 \tag{31}$$

The pressure gradient, G uses cell-centered derivatives. The merits of an approximate versus discrete expression for the divergence are discussed in detail in Almgren et al. (1996).

The integration of the above discrete equations is evaluated through a simple predictor-corrector algorithm:

1. Compute the forcing H^n at t^n.

2. Compute edge-based midpoint momenta $\vec{M}^m$ via an upwinding process. This is the predictor part of the algorithm. It uses a locally second-order discretization of Eq. 23 to extrapolate velocities from t^n to $t^{n+\frac{1}{2}}$ and interpolates velocities to the center of cell faces. This step enables advection to be computed in a second-order manner.

3. Compute advective tendencies $D^m(\vec{M}^m \psi^a)/\rho_0$ where ψ is any advected quantity and ψ^a is an edge based quantity found by third-order upwinding as described in Stevens and Bretherton (1997). In that study, this upwinding is compared to several other advection methods commonly used in meteorology. Quantities are updated from $(\vec{U}^n, \psi^n)$ to $(\vec{U}^*, \psi^*)$ where

$$\vec{U}^* = \vec{U}^n - \Delta t D^m(\vec{M}^m \vec{U}^a)/\rho_0 + \Delta t \left(-G\Pi^{n-\frac{1}{2}} + g(\theta_v^\#)^n \vec{k} + H_{\vec{U}}^n\right) \tag{32}$$

$$\psi^* = \psi^n - \Delta t D^m(\vec{M}^m \psi^a)/\rho_0 + \Delta t H_\psi^n$$

4. Compute the forcing H^* from $(\vec{U}^*, \psi^*)$ and apply its correction to the quantities $(\vec{U}^{**}, \psi^{n+1} = \psi^{**})$

$$\begin{aligned} \vec{U}^{**} &= \vec{U}^* + (\Delta t/2)(g(\theta_v^{\#})^*\vec{k} + H_{\vec{U}}^* - g(\theta_v^{\#})^n\vec{k} - H_{\vec{U}}^n) \\ \psi^{**} &= \psi^* + (\Delta t/2)(H_\psi^* - H_\psi^n) \end{aligned} \tag{33}$$

5. At the end of the timestep enforce the nodal divergence condition by solving an equation for ϕ the update to $\Pi^{n+\frac{1}{2}} = \Pi^{n-\frac{1}{2}} + \phi$.

$$D\left(\rho_0\left(\frac{\vec{U}^{**} - \vec{U}^n}{\Delta t} - G\phi\right)\right) = 0, \tag{34}$$

and applying the pressure correction

$$\vec{U}^{n+1} = \vec{U}^{**} - \Delta t G\phi, \tag{35}$$

The cell-centered discretization has several advantages over traditional staggered grid methods. The cell centered velocities and scalars make discretizing model physics much simpler. For instance, no interpolation is required for computing Coriolis forces or buoyancy terms. Model statistics are simpler to compute in a cell-centered forward-in-time model, due to the lack of averaging required to construct covariances such as fluxes and skewness. One useful property of this discretization is the ease by which discrete budgets of variance and skewness are constructed. From the temporal discretization, a typical advected quantity such as vertical velocity w satisfies:

$$\frac{\left(w^{n+1}\right)^2/2 - \left(w^n\right)^2/2}{\Delta t} = \left(\frac{w^{n+1} + w^n}{2}\right)\left(-D^m(\vec{M}^m w^a)/\rho_0 + (H_w^n + H_w^*)/2\right) \tag{36}$$

$$\frac{\left(w^{n+1}\right)^3 - \left(w^n\right)^3}{\Delta t} = \left(w^{n+1}w^{n+1} + w^n w^{n+1} + w^n w^n\right)\left(-D^m(\vec{M}^m w^a)/\rho_0 + (H_w^n + H_w^*)/2\right) \tag{37}$$

A discretely conserved kinetic energy budget $e = (u^2 + v^2 + w^2)/2$ is given by

$$\frac{e^{n+1} - e^n}{\Delta t} = \left(\frac{\vec{U}^{n+1} + \vec{U}^n}{2}\right) \bullet \left(-D^m(\vec{M}^m\vec{U}^a)/\rho_0 - \nabla\Pi^{n+\frac{1}{2}} + (g/2)((\theta_v^{\#})^n + (\theta_v^{\#})^*)\vec{k} + (H_{\vec{U}}^n + H_{\vec{U}}^*)/2\right) \tag{38}$$

This requires no manipulation of the buoyancy as is often done in the budgets of staggered discretizations.

REFERENCES

Almgren, A. S., J. B. Bell, and W. G. Szymczak, 1996: A numerical method for the incompressible Navier-Stokes equations based on an approximate projection. *SIAM J. Sci. Comput.*, **17**(2).

Almgren, A. S., J. B. Bell, P. Colella, L. H. Howell, and M. L. Welcome, 1998: A Conservative Adaptive Projection Method for the Variable Density Incompressible Navier-Stokes Equations, *J. Comp. Phys.*, To Appear.

Bell, J. B., D. L. Marcus, 1992: Vorticity intensification and transition to turbulence in the three-dimensional Euler equations. *Commun. Math. Phys.*, **147**, 371-394.

Bretherton, C. S., M. K. MacVean, P. Becthtold, A. Chlond, W. R. Cotton, J. Cuxart, H. Cjuipers, M. Khairoutdinov, B. Kosovic, D. Lewellen, C. H. Moeng, P. Siebesma, B. Stevens, D. E. Stevens, R. I. Sykes, and M. C. Wyant, 1998: An intercomparison of radiatively-driven entrainment and turbulence in a smoke cloud, as simulated by different numerical models. *Quart. J. R. Meteor. Soc.*, To Appear.

Brown, D. L., and M. L. Minion, 1995: Performance and under-resolved two-dimensional incompressible flow simulations *J. Comp. Phys.*, **122**, 165-183.

Chorin, A. J., 1986: Turbulence and vortex stretching on a lattice. *Commun. Pure Appl. Math.*, **39**, 47-65.

Deardorff, J. W., 1980: Cloud-top entrainment instability *J. Atmos. Sci.*, **37**, 131-147.

Flatau, P.J., R. L. Walko, and W. R. Cotton, 1992: Polynomial fits to saturation vapor pressure. *J. Appl. Met.*, **31**, No. 12, 1507-13.

Kuo, H., and W. T. Schubert, 1988: Stability of cloud-topped boundary layers. *Quart. J. R. Meteor. Soc.*, **114**, 887-916.

LeVeque, R. L., 1992: Numerical Methods for Conservation Laws, *Birkhauser Verlag*, Boston.

Lewellen, D. C., and W. S. Lewellen, 1998: Large eddy boundary layer entrainment. *J. Atmos. Sci.*, Submitted.

Lilly, D. K., 1962: On the numerical simulation of buoyant convection. *Tellus*, **14**, 148-171.

Lock, A. P., and M. K. MacVean, 1997: The parameterization of entrainment driven by surface heading and cloud-top cooling. *Quart. J. R. Meteor. Soc.*, Submitted.

MacVean, M. K., and P. J. Mason, 1990: Cloud-top entrainment instability through small-scale mixing and its parameterization in numerical models, *J. Atmos. Sci.*, **47**, 1012-1030.

MacVean, M. K., and C. S. Bretherton, 1998: Boundary-layer cloudiness and cloud-top entrainment instability – a new synthesis. *Quart. J. R. Meteor. Soc.*, Submitted.

Mason, P. J., and A. R. Brown, 1994: The sensitivity of large-eddy simulations of turbulent shear flow to subgrid models. *Bound. Layer Meteor.*. **70**, 133-150.

Mason, P. J., and A. R. Brown, 1998: On Subgrid models and filter operations in large-eddy simulations. *J. Atmos. Sci.*, Provisionally Accepted.

McEwan, A. D., and G. W. Paltridge, 1976: Radiatively driven thermal convection bounded by an inversion - a laboratory simulation of stratus clouds. *J. Geophys. Res.*, **81**, 1095-1102.

Mellor, G. L. and T. Yamada, 1974: A Hierarchy of Turbulence Closure Models for Planetary Boundary

Layers, *J. Atmos. Sci.*, **31**, 1791-1806.

Moeng, C.-H., W. R. Cotton, C. S. Bretherton, A. Chlond, M. Khairoutdinov, S. Krueger, W. S. Lewellen, M. K. MacVean, J. R. M. Pasquier, H. A. Rand, A. P. Siebesma, R. I. Sykes, and B. Stevens, 1995: Simulation of a stratocumulus-topped PBL: Intercomparison among different numerical codes. *Bull. Amer. Meteor. Soc.*, **77**, 261-278.

Nicholls, S., and J. D. Turton, 1986: An observational study of the structure of stratiform cloud sheets: Part II. Entrainment. *Quart. J. R. Meteor. Soc.*, **112**, 461-480.

Ogura, Y., and N. Phillips, 1962: Scale Analysis of Deep and Shallow Convection in the Atmosphere. *J. Atmos. Sci.*, **19**, 173-179.

Rendleman, C. A., V. E. Beckner, M. Lijewski, W. Crutchfield, and J. B. Bell, 1998.: A parallel adaptive mesh refinement algorithm for the simulation of explosions. In Preparation.

Randall, D. A., 1980: Conditional instability of the first kind upside-down. *J. Atmos. Sci.*, **37**, 125-130.

Sayler, B. J., 1996: *Laboratory simulations of radiatively induced entrainment in stratiform clouds.* Ph. D. dissertation, University of Washington, 181 pp. Available from the Department of Atmospheric Science, Box 351640, University of Washington, Seattle, WA 98195.

Siems, S. T., C. S. Bretherton, M. B. Baker, S. Shy, and R. E. Breidenthal, 1990: A numerical investigation of cloud-top entrainment instability and related experiments. *Quart. J. R. Meteor. Soc.*, **118**, 787-818.

Skamarock, W. C., and J. B. Klemp, 1993: Adaptive grid refinement for two-dimensional and three-dimensional nonhydrostatic atmospheric flow. *Monthly Weather Review*, **121**, No. 3, 788-804.

Smagorinsky, J., 1963: General circulation experiments with the primitive equations: 1. The basic experiment. *Monthly Weather Review*, **91**, 99-164.

Smolarkiewicz, P. K. and L. G. Margolin, 1993: On forward-in-time differencing for fluids: extension to a curvilinear framework. *Monthly Weather Review*, **121**, No. 6, 1847-1859.

Stevens, B. C. H. Moeng, and P. P. Sullivan, 1998: Subgrid sensitivities in large-eddy simulations of radiatively driven convection. *J. Atmos. Sci.*, submitted.

Stevens, D. E. and C. S. Bretherton, 1997: A forward-in-time advection scheme and adaptive multilevel flow solver for nearly incompressible atmospheric flow. *J. Comput. Phys.*, **129**, 284-295.

Stevens, D. E. and C. S. Bretherton, 1998: Effects of Grid Resolution on Large-Eddy Simulation of Radiatively Driven Entrainment Through A Strong Inversion. Quart. J. Roy. Met. Soc.. To Appear.

Stevens, D. E., A. S. Almgren, J. B. Bell, V. E. Beckner, and Charles A. Rendleman, 1998: Effects of mesh refinement on the simulation of trade cumulus convection. *Mon. Wea. Rev.*, In preparation.

Stull, R. B., 1976: The energetics of entrainment across a density interface. *J. Atmos. Sci.*, **33**, 1260-1267.

Turner, J. S., 1968: The influence of molecular diffusivity on turbulent entrainment across a density interface. *J. Fluid Mech.*, **33**, 639-656.

Simulation	smoke	slopes	sgs	NX	NZ	Δx (m)	Δz (m)	λ (m)
L00S_00	no	yes	none	64	48	50.00	25.00	40
M00S_00	no	yes	none	128	96	25.00	12.50	20
H00S_00	no	yes	none	256	192	12.50	6.25	10
L40S_15	no	yes	TKE	64	48	50.00	25.00	40
M20S_15	no	yes	TKE	128	96	25.00	12.50	20
H10S_15	no	yes	TKE	256	192	12.50	6.25	10
L00_00	no	no	none	64	48	50.00	25.00	40
M00_00	no	no	none	128	96	25.00	12.50	20
H00_00	no	no	none	256	192	12.50	6.25	10
L40_10	no	no	SMAG	64	48	50.00	25.00	40
M20_10	no	no	SMAG	128	96	25.00	12.50	20
H10_10	no	no	SMAG	256	192	12.50	6.25	10
L40_15	no	no	TKE	64	48	50.00	25.00	40
M20_15	no	no	TKE	128	96	25.00	12.50	20
H10_15	no	no	TKE	256	192	12.50	6.25	10
V06_15	no	no	TKE	400	300	8.00	4.00	6
SL40_15	yes	no	TKE	64	48	50.00	25.00	40
SM20_15	yes	no	TKE	128	96	25.00	12.50	20
SH10_15	yes	no	TKE	256	192	12.50	6.25	10

Table 1: Simulation names are a combination of smoke (S), resolution (L,M,H,V), Smagorinsky length scale ($\lambda = (\Delta x \Delta y \Delta z)^{1/3}$) in meters, slope limiting (S_) and the order of the subgrid model. TKE and SMAG are acronyms for the turbulent kinetic energy and Smagorinsky subgrid models respectively.

Simulation	A	w_e (mm/s)	w^* (m/s)	δz_u (m)	δz_{inv} (m)	std. δz_{inv} (m)
L00S_00	1.00	9.56	1.01	7.19	16.53	9.78
M00S_00	1.02	9.59	1.00	7.09	10.91	8.90
H00S_00	1.01	9.71	1.01	7.22	7.89	8.87
L40S_15	1.02	9.32	1.00	7.02	16.63	9.91
M20S_15	1.00	9.41	1.01	7.11	10.74	8.98
H10S_15	1.04	9.63	1.00	7.04	7.97	8.60
L00_00	1.13	10.69	1.00	7.23	17.29	10.33
M00_00	1.23	11.27	0.99	7.00	11.15	8.93
H00_00	1.19	11.41	1.00	7.23	8.13	9.36
L40_10	1.12	10.57	1.00	7.20	17.06	10.35
M20_10	1.13	10.55	1.00	7.09	10.97	8.48
H10_10	1.15	10.85	1.00	7.15	8.01	8.44
L40_15	1.13	10.62	1.00	7.18	17.12	10.20
M20_15	1.13	10.42	0.99	7.03	10.93	8.91
H10_15	1.19	11.03	0.99	7.08	8.17	9.57
V06_15	1.22	11.07	0.99	7.00	6.82	9.83
SL40_15	0.71	4.63	1.03	4.28	20.78	5.18
SM20_15	0.67	4.59	1.05	4.40	14.80	4.78
SH10_15	0.61	4.34	1.06	4.52	12.05	5.16

Table 2: Simulation parameters after 2.5 hours of simulation.

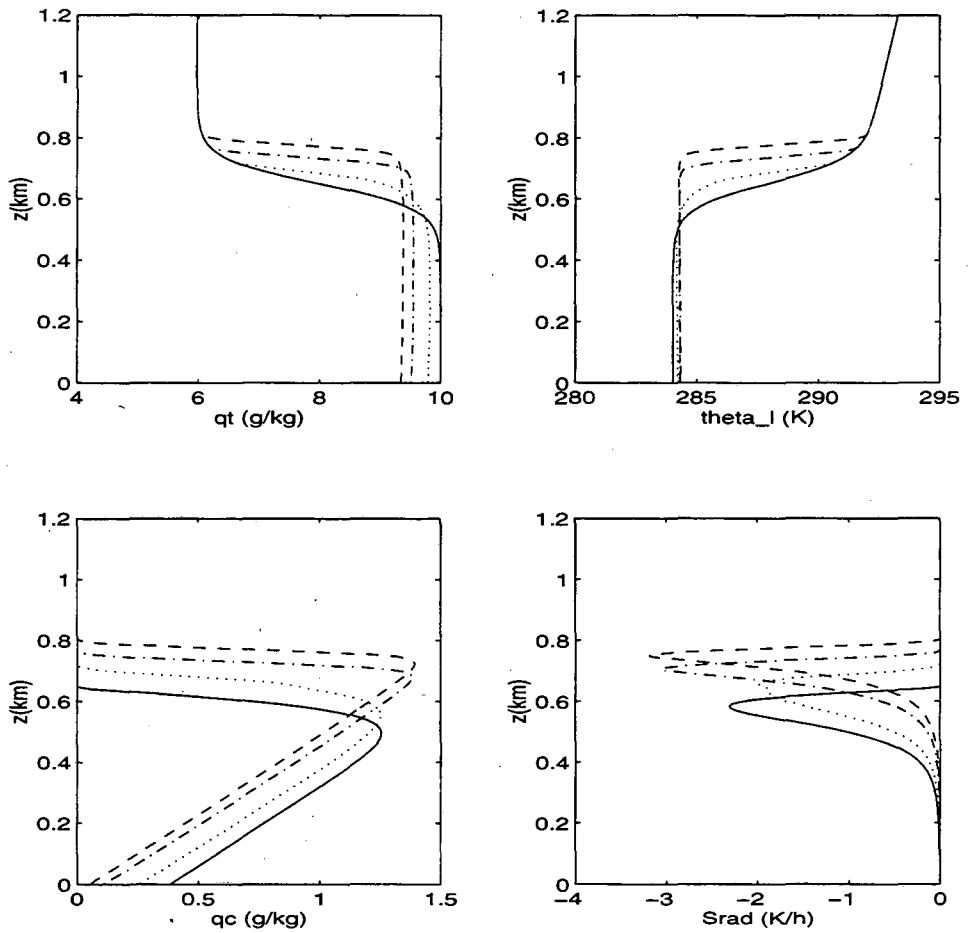

Figure 1: Initial Conditions (solid). 1 hour averages centered at: dotted, 30 minutes; dash-dot, 90 minutes; and dashed, 150 minutes. S_{rad} is the radiative flux divergence

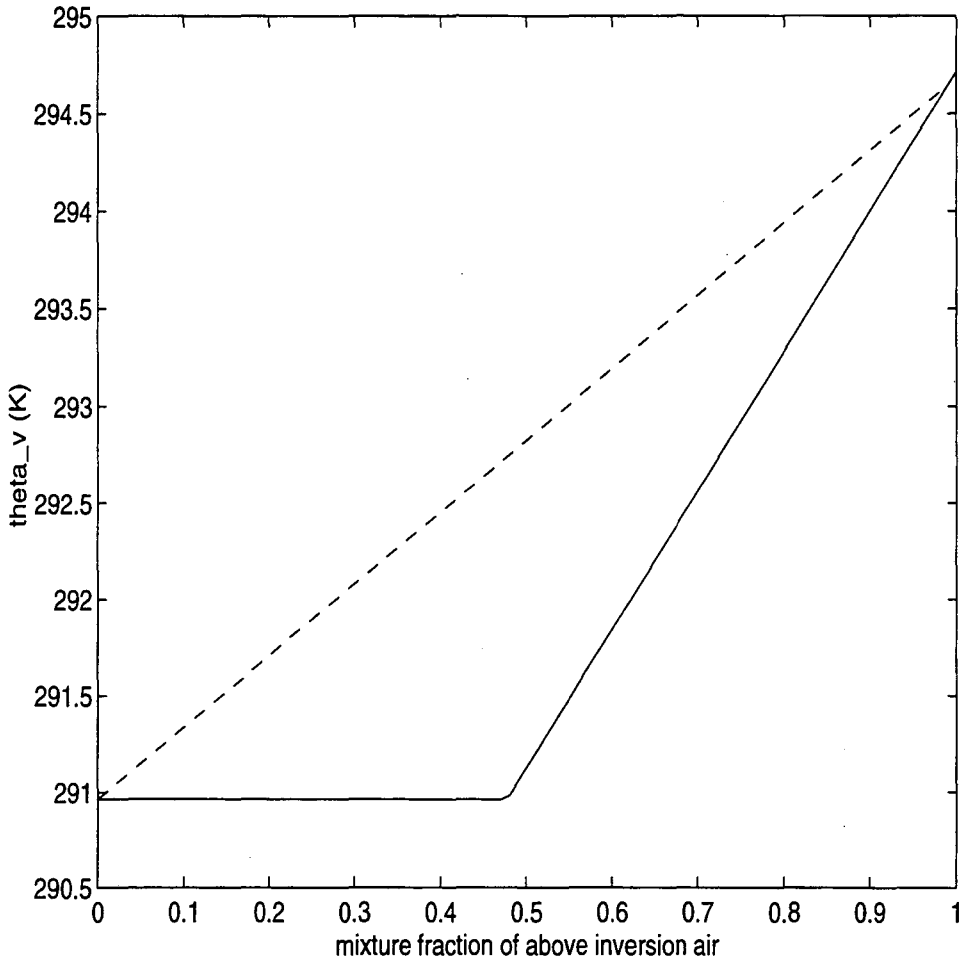

Figure 2: Buoyancy for mixtures as a function of mixing fraction of above inversion air. This is shown as a solid line. The bouyancy of these mixtures if no evaporative cooling is present is shown as a dashed line.

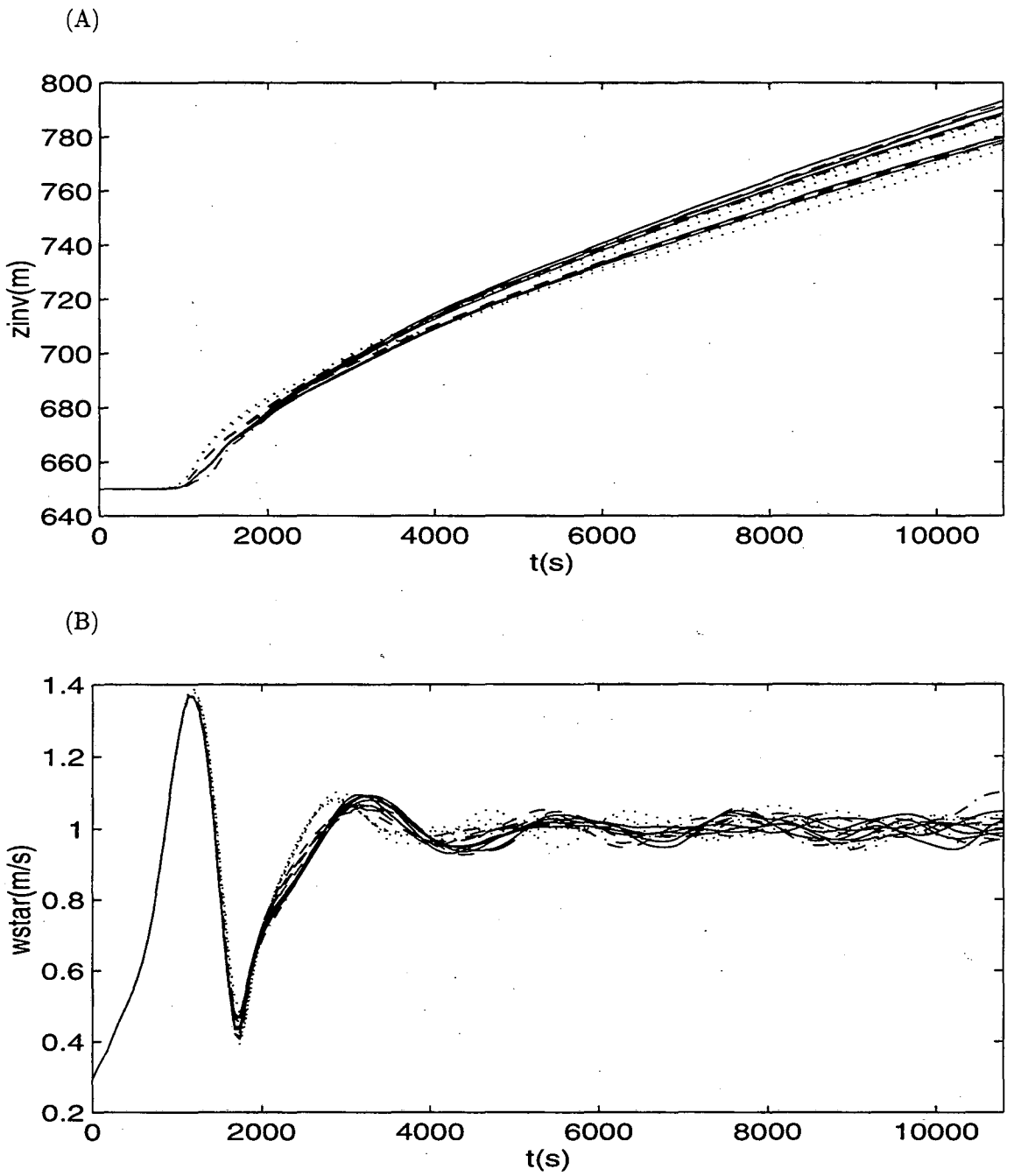

Figure 3: Inversion height z_{inv} (A) and w^* (B) as functions of time. Line types are determined by resolution L (dot), M (dash), H (solid), and V (dash-dot).

(A)

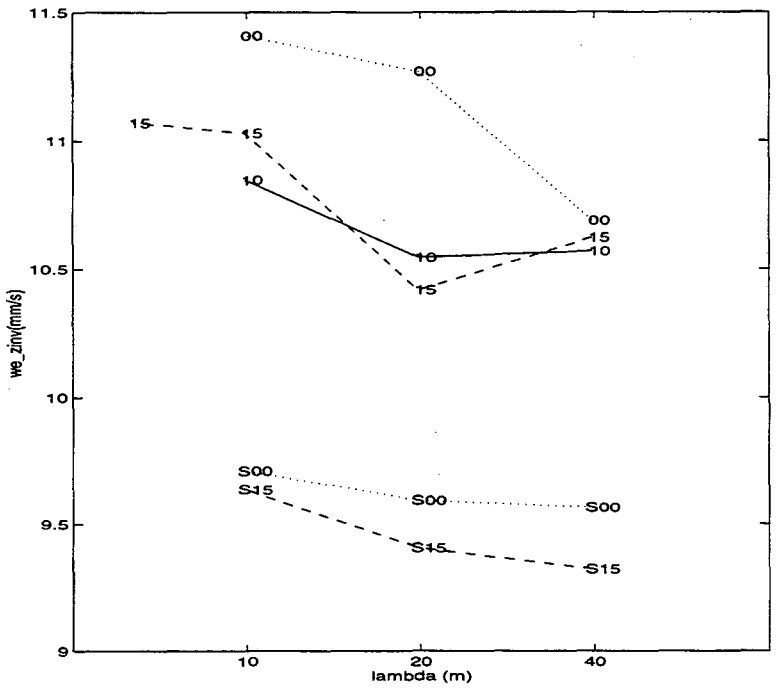

(B)

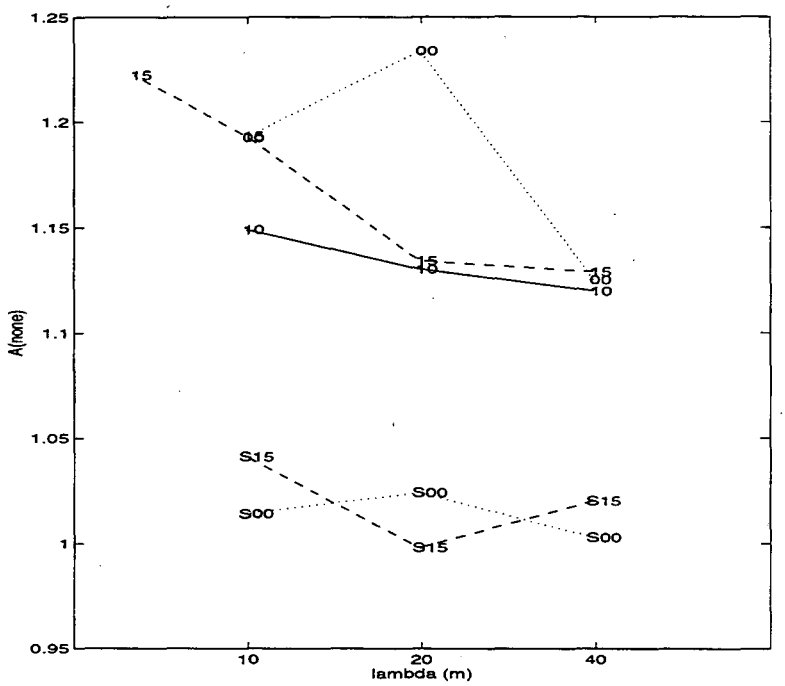

Figure 4: w_e (A) and the A parameter (B). Line types are determined by subgrid model used: none (dots), Smagorinsky (solid) and TKE (dashs). Data points are labeled with the order of their sub-grid model and are preceded by an S when slope-limiting is present.

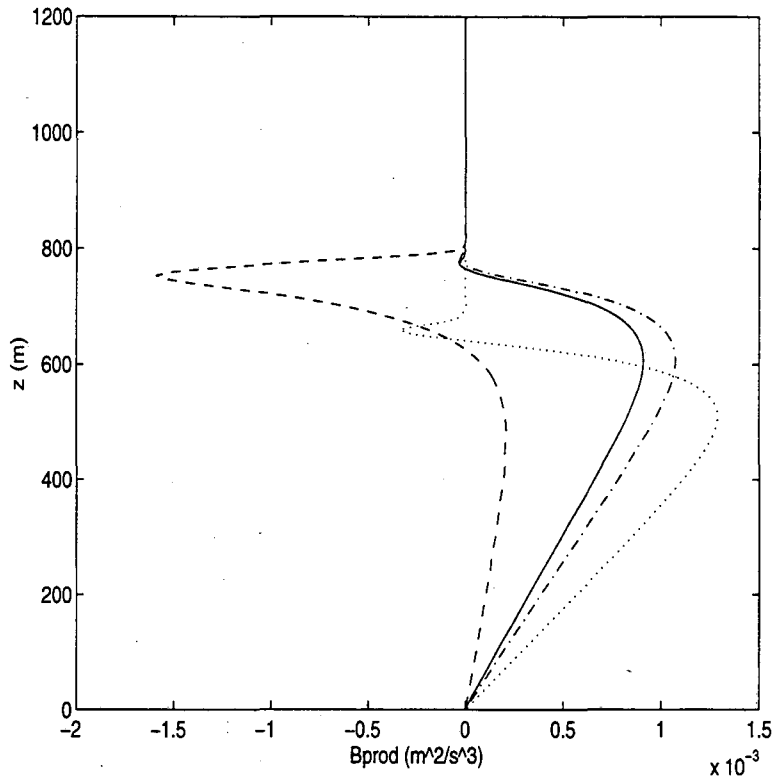

Figure 5: Buoyancy flux comparison. Estimated unsaturated buoyancy flux (dash), estimated saturated buoyancy flux (dash-dot), and actual buoyancy flux (solid) for the simulation **H10_15**. The smoke simulation **SH10_15** is shown for comparison (dot).

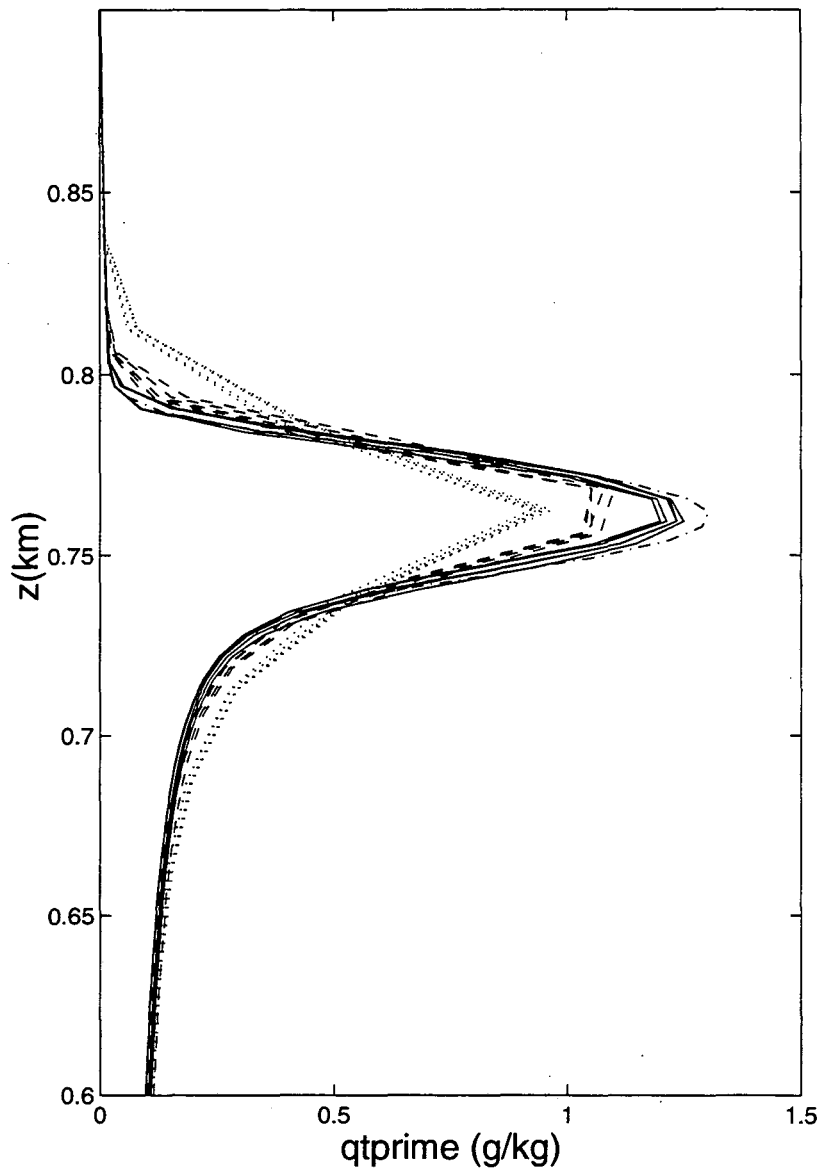

Figure 6: $\left(\overline{q_t'^2}\right)^{1/2}$ at the inversion. Line types are determined by resolution L (dot), M (dash), H (solid), and V (dash-dot).

(A)

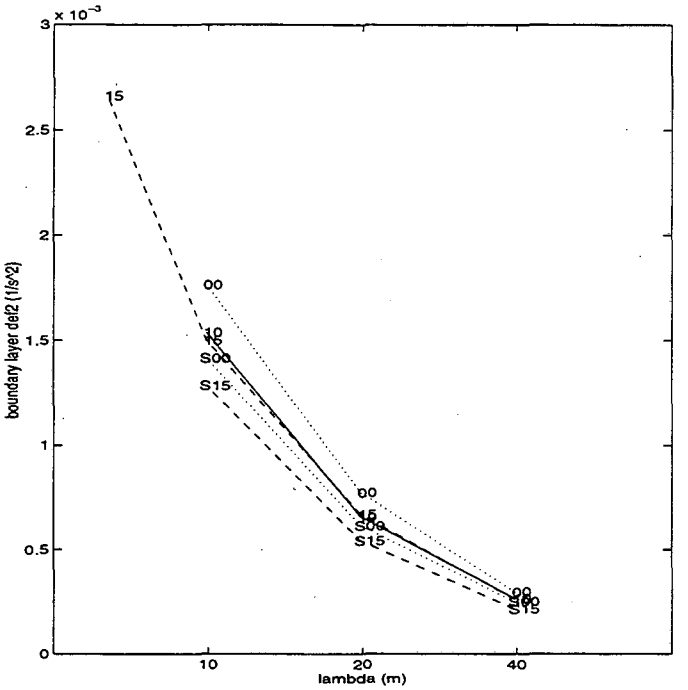

(B)

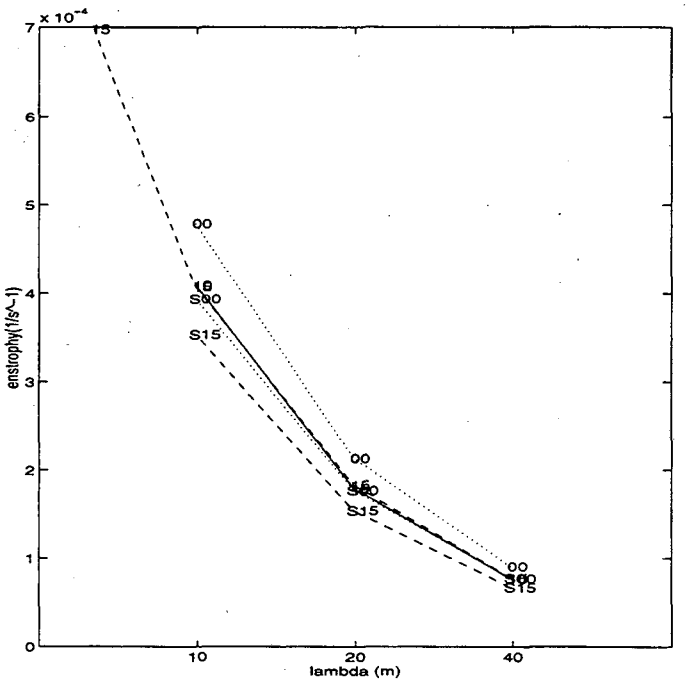

Figure 7: Boundary layer deformation (A) and enstrophy (B). Curves are labeled as in Figure 4.

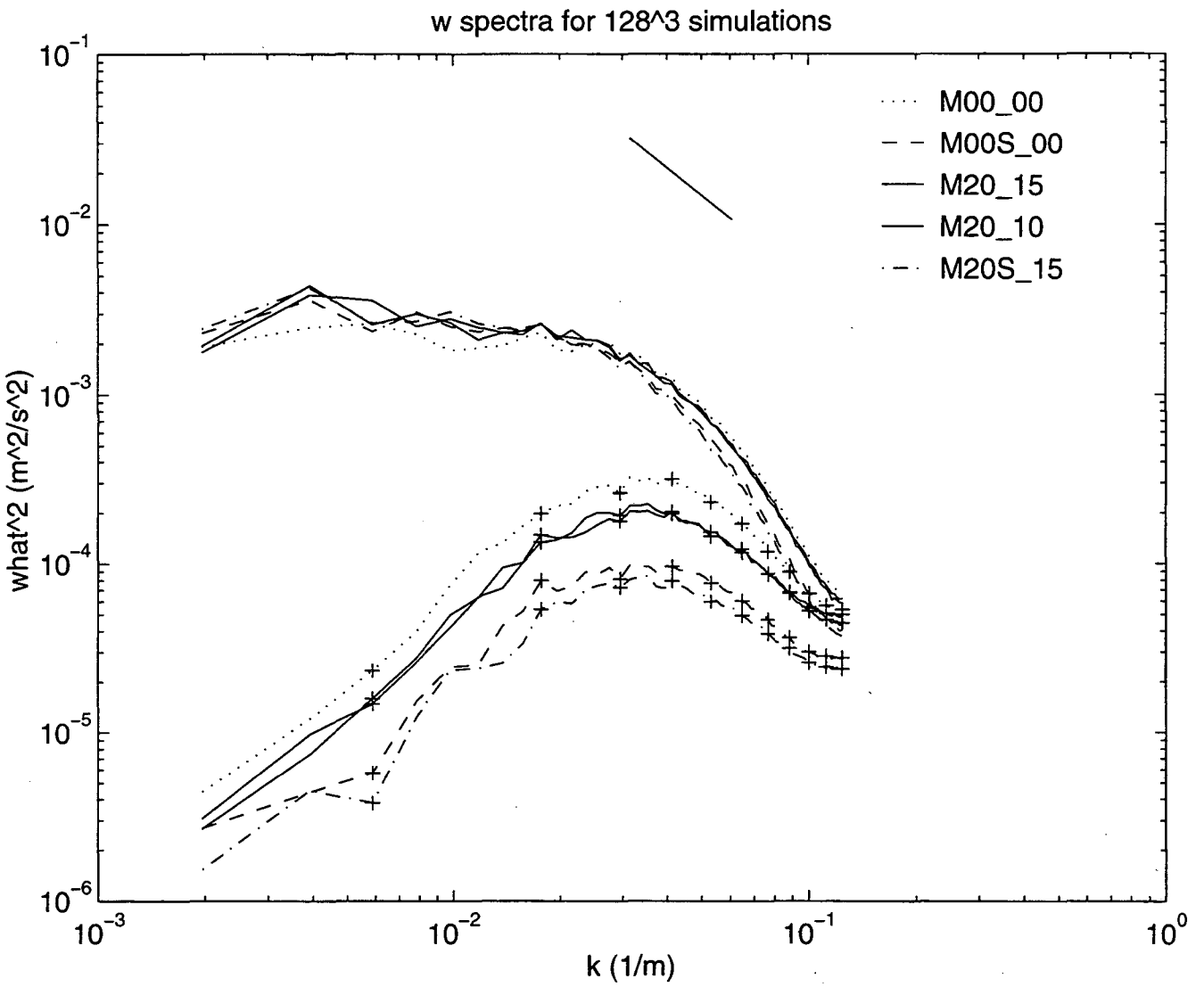

Figure 8: Sensitivity of power spectra of w to numerics. Spectra denoted by + symbols are calculated from data at the inversion. Spectra without the + symbols are calculated from data at the middle of the boundary layer. The straight solid line has a slope of $k^{-5/3}$.

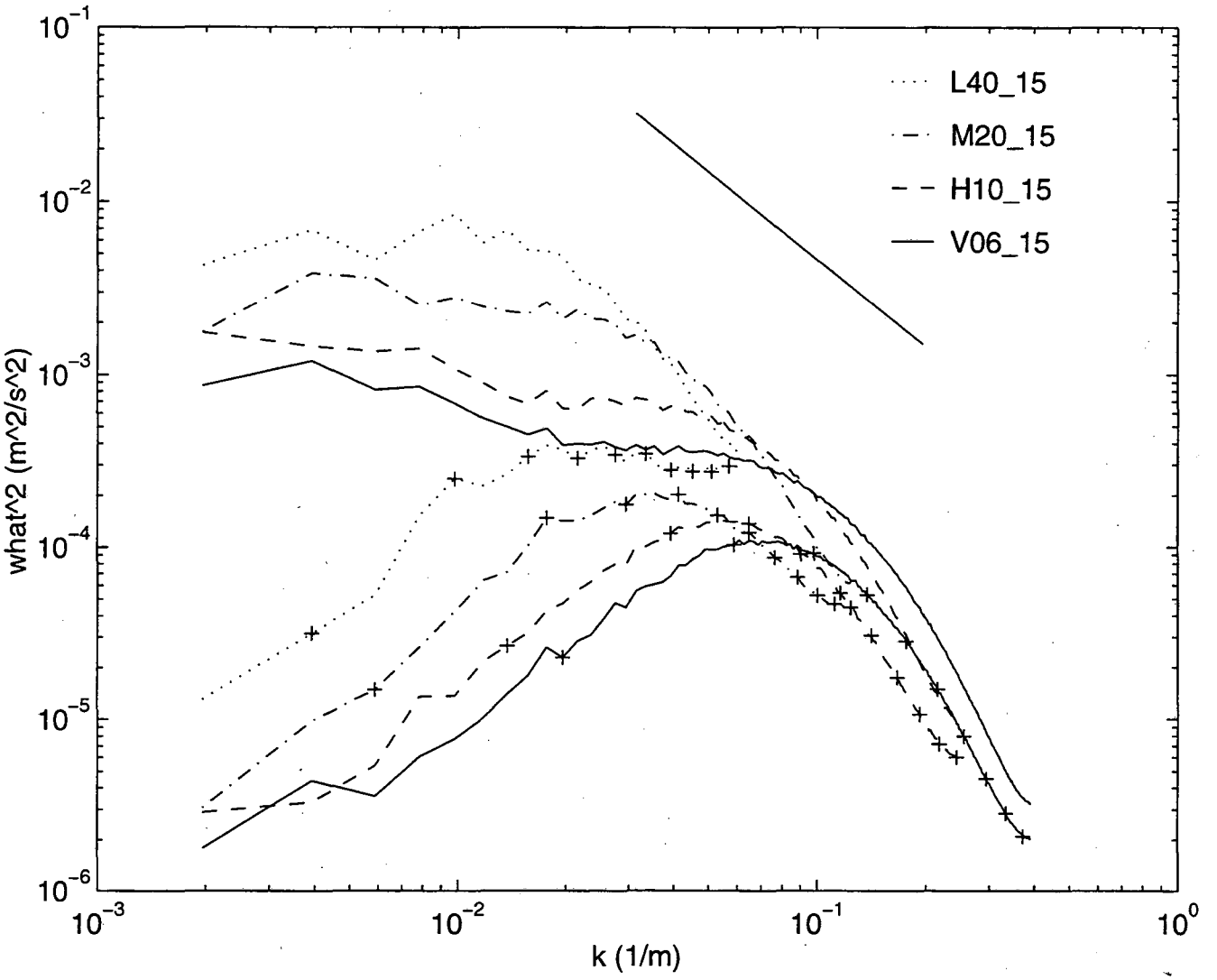

Figure 9: Sensitivity of power spectra of w to resolution. Spectra denoted by + symbols are calculated from data at the inversion. Spectra without the + symbols are calculated from data at the middle of the boundary layer. The straight solid line has a slope of $k^{-5/3}$.

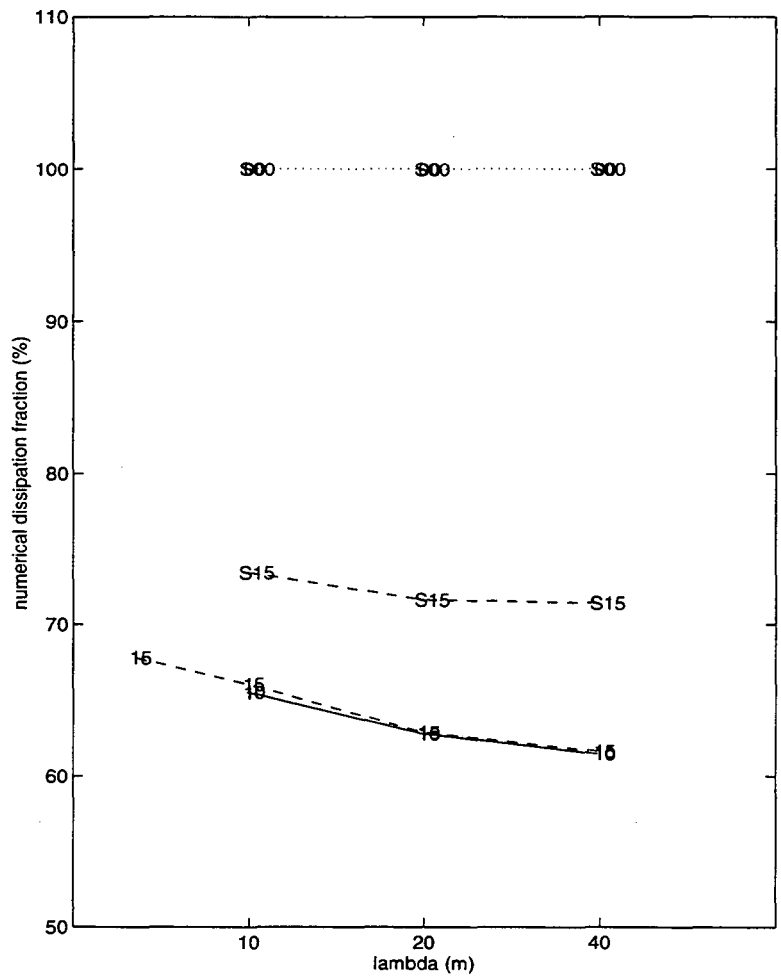

Figure 10: Percentage of total dissipation which is numerical. Curves are labeled as in Figure 4.

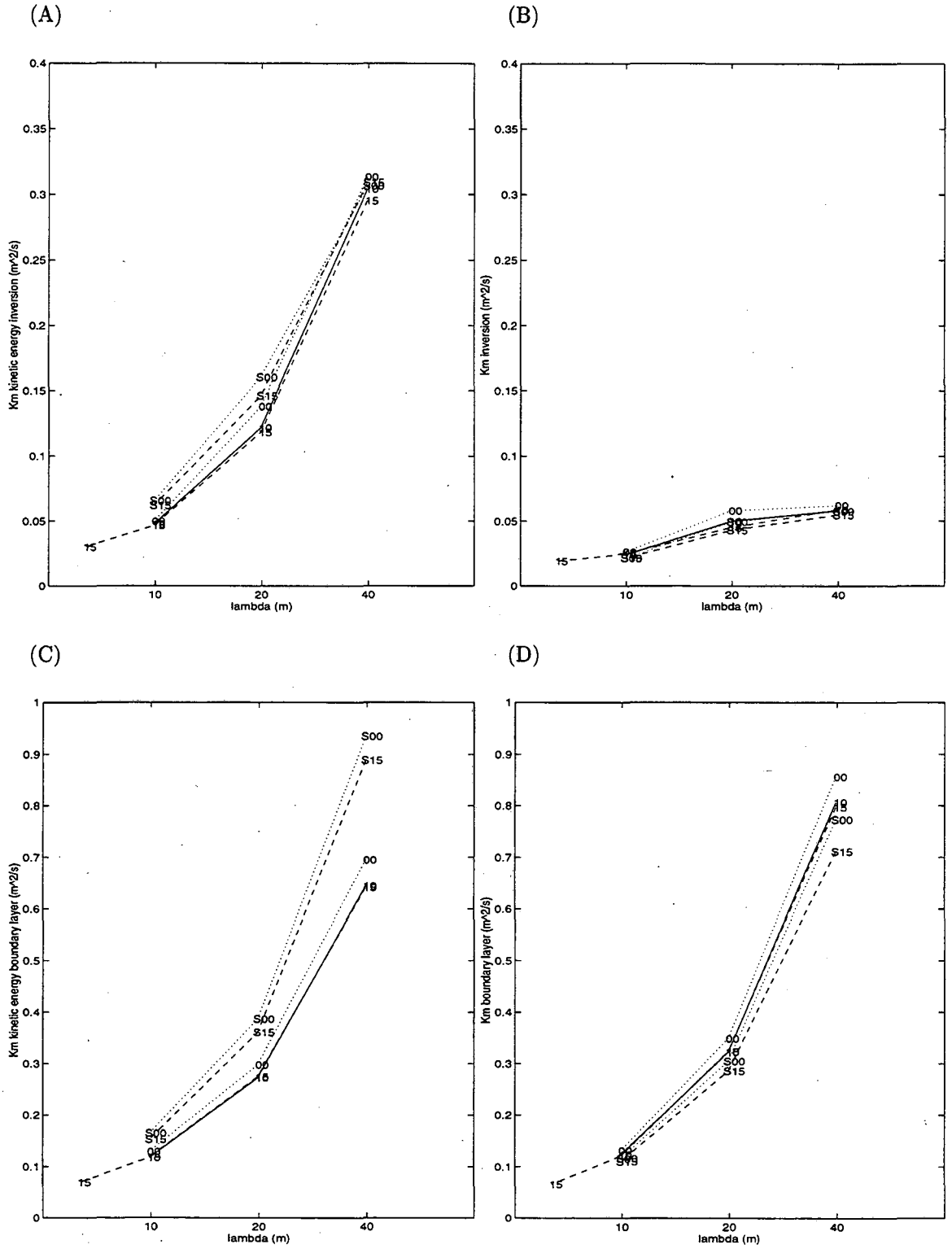

Figure 11: Eddy viscosity comparison: K_e at the inversion (A), K_m at the inversion (B), K_e in the boundary layer (C), and K_m in the boundary layer (D). Curves are labeled as in Figure 4.

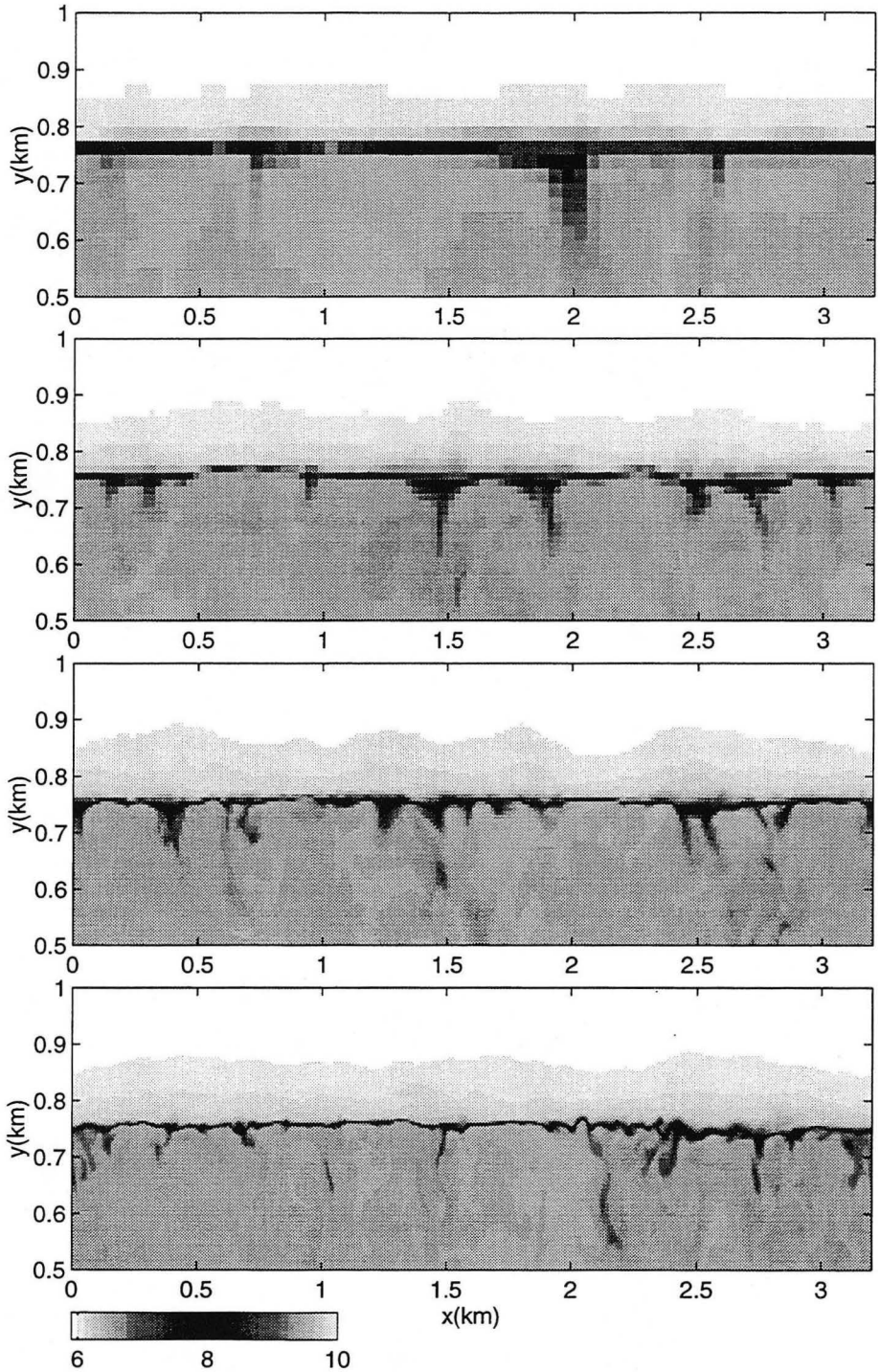

Figure 12: qt cross section in (g/kg) at t = 2 hours. L40_15 (top), M20_15 (upper middle), H10_15 (lower middle), and V06_15 (bottom).

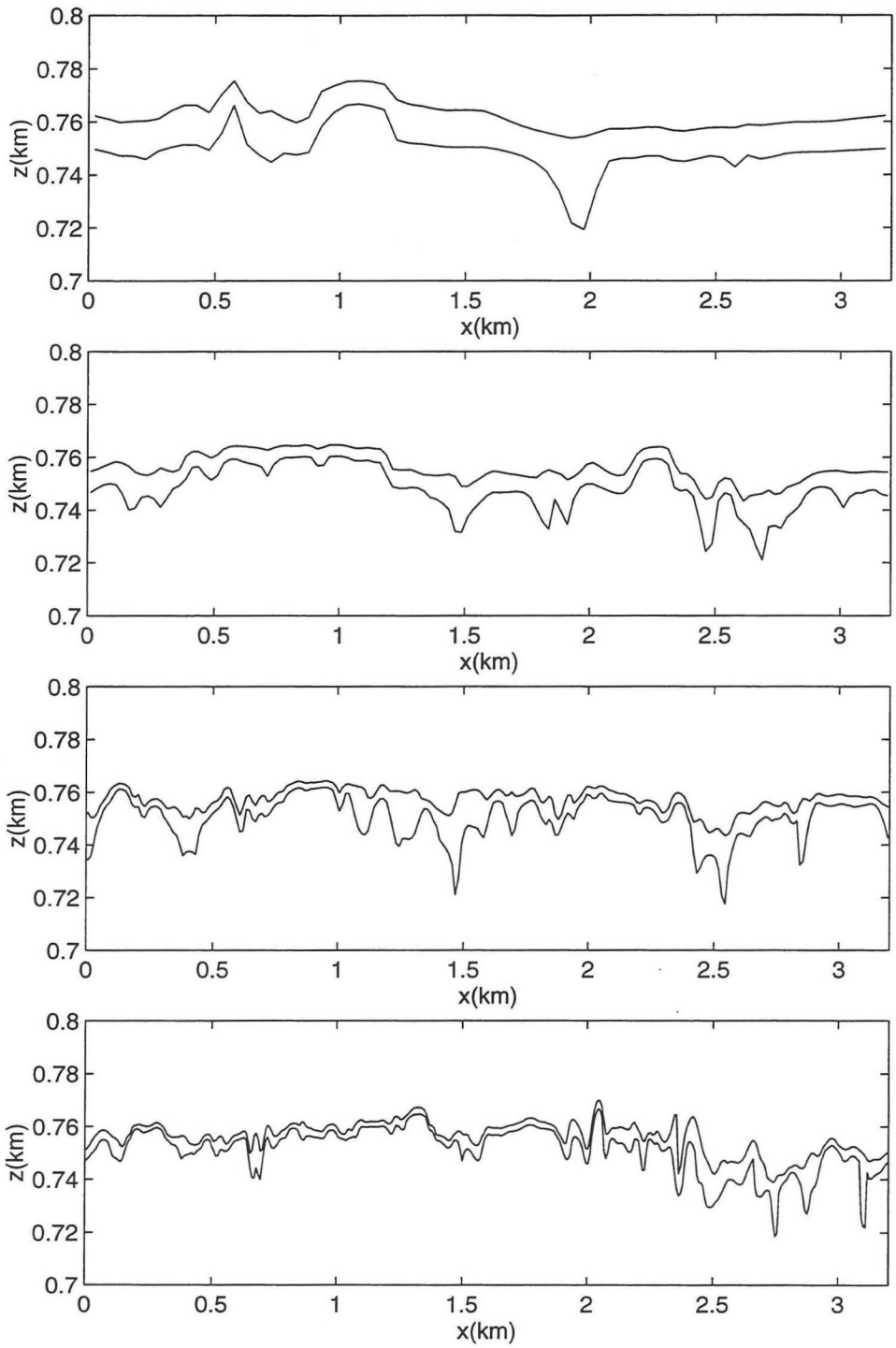

Figure 13: Cross section showing δz_{inv} at t = 2 hours. This quantity is a measure of boundary layer thickness. L40_15 (top), M20_15 (upper middle), H10_15 (lower middle), and V06_15 (bottom).

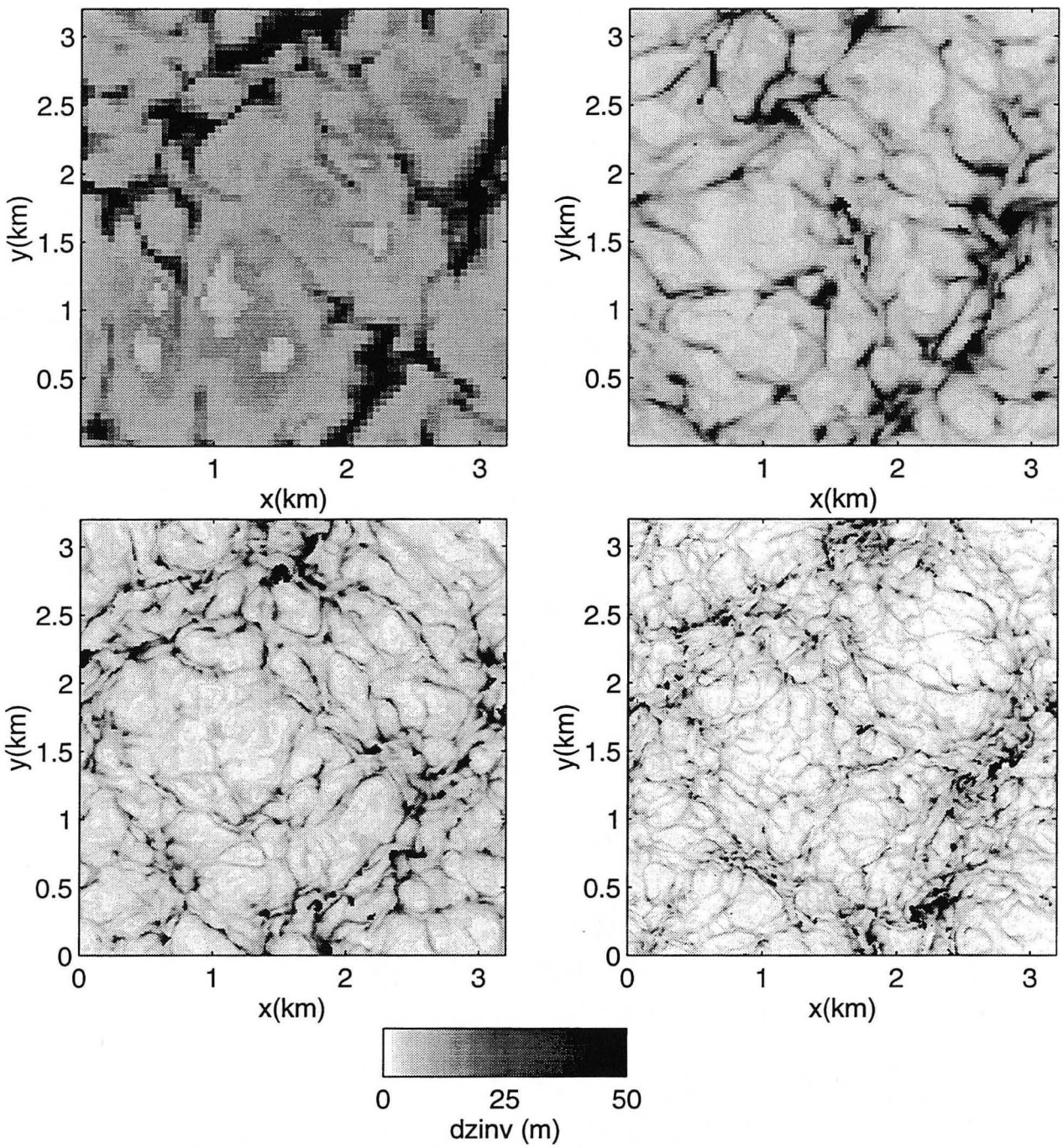

Figure 14: δz_{inv} for each resolution at t = 2 hours. (top left, L40_15; top right, M20_15; bottom left, H10_15; bottom right, V06_15)

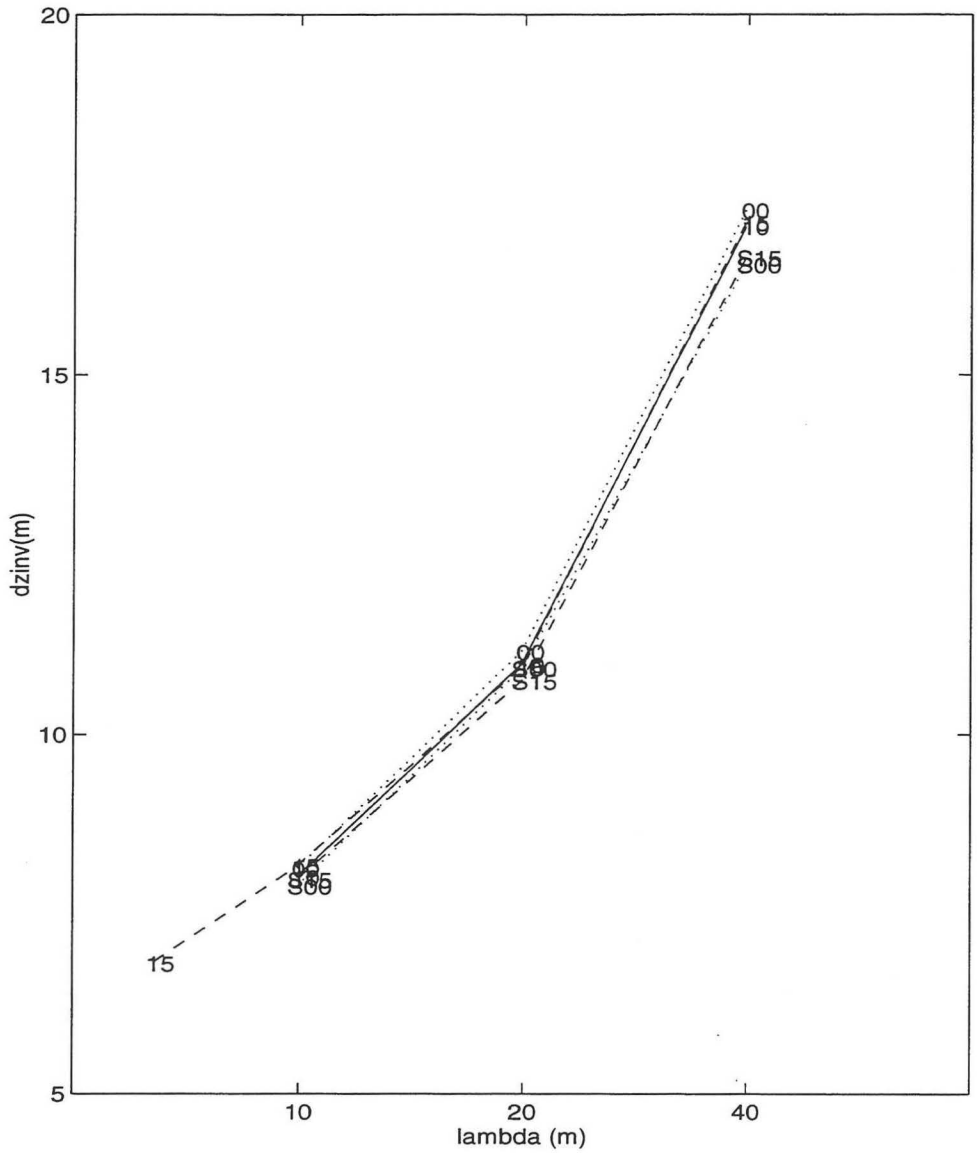

Figure 15: δz_{inv} convergence as a function of resolution. Curves are labeled as in Figure 4.

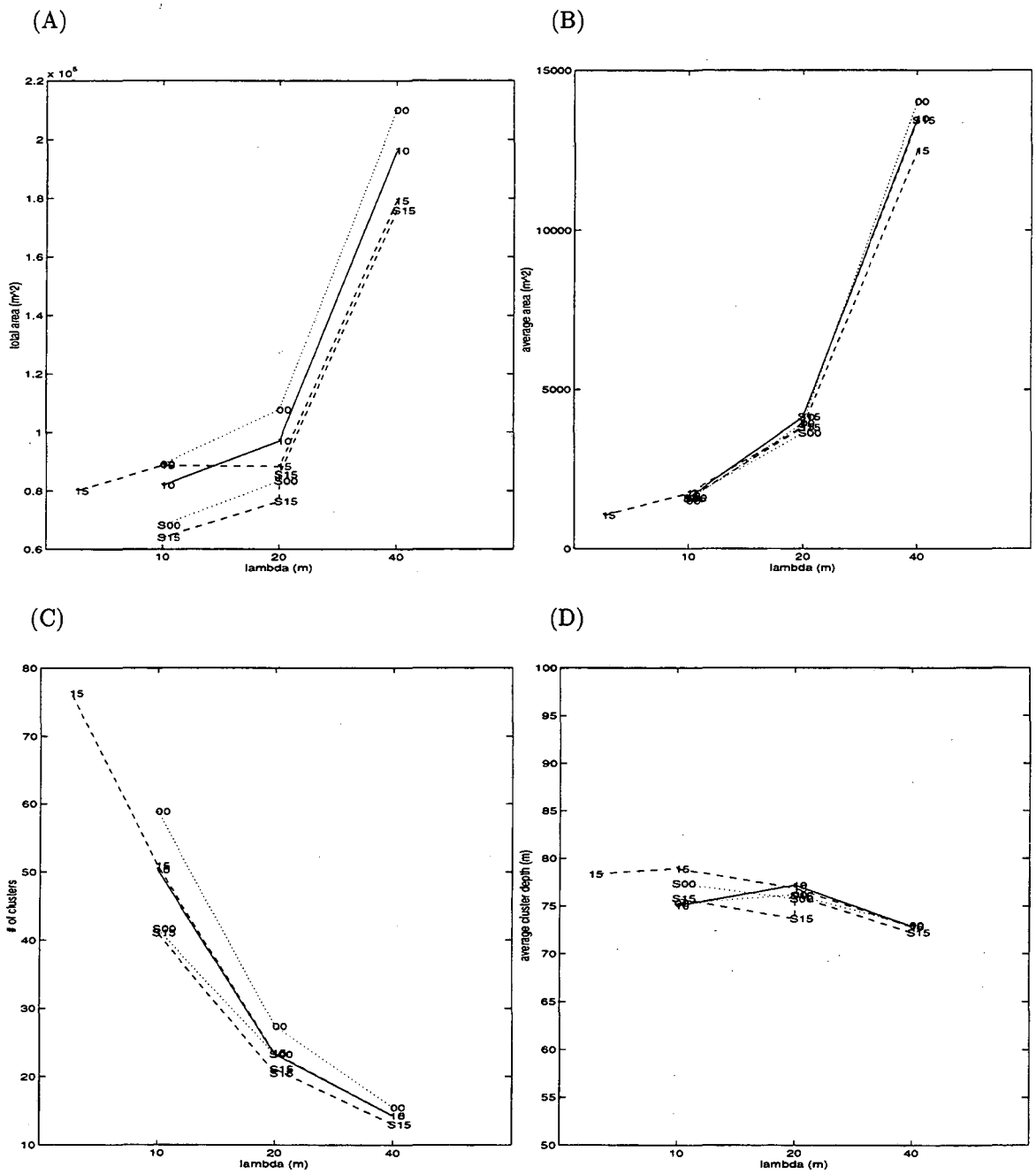

Figure 16: Total area (A), average area (B), number (C) and average depth (D) of clusters. Curves are labeled as in Figure 4.

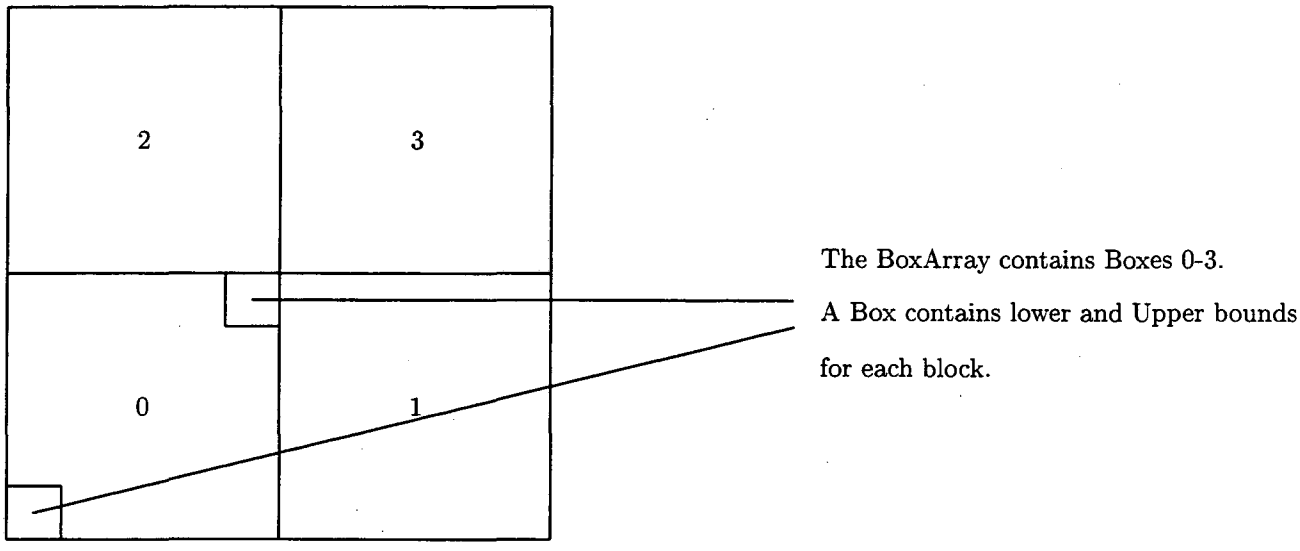

Figure 17: Schematic of BoxLib abstractions describing a BoxArray.

Ernest Orlando Lawrence Berkeley National Laboratory
One Cyclotron Road | Berkeley, California 94720

Prepared for the U.S. Department of Energy under Contract No. DE-AC03-76SF00098